Editors' Suggestion

Framework for polarized magnetic neutron scattering from nanoparticle assemblies with vortex-type spin textures

Michael P. Adams,* Evelyn P. Sinaga, Štefan Liščák, and Andreas Michels†
Department of Physics and Materials Science, University of Luxembourg, 162A Avenue de la Faiencerie, L-1511 Luxembourg, Grand Duchy of Luxembourg

(Received 25 April 2024; revised 26 June 2024; accepted 27 June 2024; published 12 July 2024)

Within the framework of the recently introduced multinanoparticle power-series expansion method for the polarized small-angle neutron scattering (SANS) cross section, we present analytical expressions for the polarized SANS observables arising from dilute nanoparticle assemblies with antisymmetric vortex-type spin structures. We establish connections between the magnetic correlation coefficients and the magnetic field-dependent vortex-axes distribution function, which is related to the random orientations of the magnetocrystalline anisotropy axes of the nanoparticles. Our analytical results are validated through a comparative analysis with micromagnetic simulations. This framework contributes to a comprehensive understanding of polarized magnetic neutron scattering from spherical nanoparticle systems exhibiting vortex-type spin structures.

DOI: 10.1103/PhysRevB.110.014420

I. INTRODUCTION

Magnetic nanoparticles, which are within the scope of immense interdisciplinary research, offer versatile applications, e.g., in materials science, nanotechnology, and biomedicine [1–7]. They open up new possibilities in the nanoscopic realm and drive technological advances and breakthrough discoveries. But still, at the current stage of research, it is an immense challenge to characterize their internal spin structure, which is generally expected to be nonuniform (e.g., [8–16]).

Magnetic small-angle neutron scattering (SANS) is possibly the only technique to probe the spatial variation of spin structures on a scale of ∼1–100 nm and in the bulk of the material [17,18]. Recent advances in the understanding of magnetic SANS from complex nanoparticle systems have been achieved by the marriage of micromagnetic theory and the magnetic neutron scattering formalism, through both computer simulations and analytical calculations [19–27]. Although computer simulations offer considerable potency in predicting neutron scattering observables for intricate nanoparticle assemblies, their drawback lies in their time-intensive nature, vast parameter space, and the inherent challenge of interpreting results. This complexity hinders the derivation of overarching conclusions and poses a substantial obstacle in formulating generalized statements.

To address these challenges, Adams *et al.* [28] introduced the multinanoparticle power-series expansion (MNPSE) method to study the neutron scattering signatures from spherical nanoparticle assemblies featuring diverse types of magnetic surface anisotropy. Here, we use the MNPSE approach to predict the main features of nanoparticle assemblies with inherent *vortex-type spin textures* such as those seen in the neutron scattering observables. Vortex-type structures are ubiquitous in magnetism research and are encountered in many systems, such as in type-II superconductors [29], $GdCo_2$ micropillars [30], Nd-Fe-B magnets [31], iron oxide nanoparticles [32–34], and nanoflowers [35], or the very recently discovered topological vortex rings in a chiral magnetic nanocylinder [36]. Our results, which replace the conventional analytical formulation for the superspin model, enable the straightforward prediction of the spin-flip SANS cross section $I_{\rm sf}(q)$ and the corresponding spin-flip pair-distance distribution function $p_{\rm sf}(r)$ arising from spatially antisymmetric spin structures, such as nanovortices, through easily applicable analytical expressions.

The paper is organized as follows: We start out by analyzing the main features of the first-order MNPSE method for the spin-flip SANS cross section and the pair-distance distribution function (Sec. II). This approach is valid for an *arbitrary linear magnetization distribution*. Subsequently, for the particular case of a *linear vortex*, we derive analytical expressions for the two- and one-dimensional SANS observables (Sec. III). The analytical expressions are compared to the results of micromagnetic computations. Section IV summarizes the main findings of this study. We refer to the Supplemental Material [37] for details regarding the analytical derivations and the micromagnetic SANS simulations (see also Refs. [38–40] therein).

II. LINEAR MNPSE METHOD

This approach is based on the following expansion for the magnetization vector field:

$$\mathbf{M}'(\mathbf{r}') = \begin{bmatrix} m_0^x \\ m_0^y \\ m_0^z \end{bmatrix} + \begin{bmatrix} m_1^{xx} & m_1^{xy} & m_1^{xz} \\ m_1^{yx} & m_1^{yy} & m_1^{yz} \\ m_1^{zx} & m_1^{zy} & m_1^{zz} \end{bmatrix} \cdot \begin{bmatrix} x' \\ y' \\ z' \end{bmatrix}, \quad (1)$$

*Contact author: michael.adams@uni.lu
†Contact author: andreas.michels@uni.lu

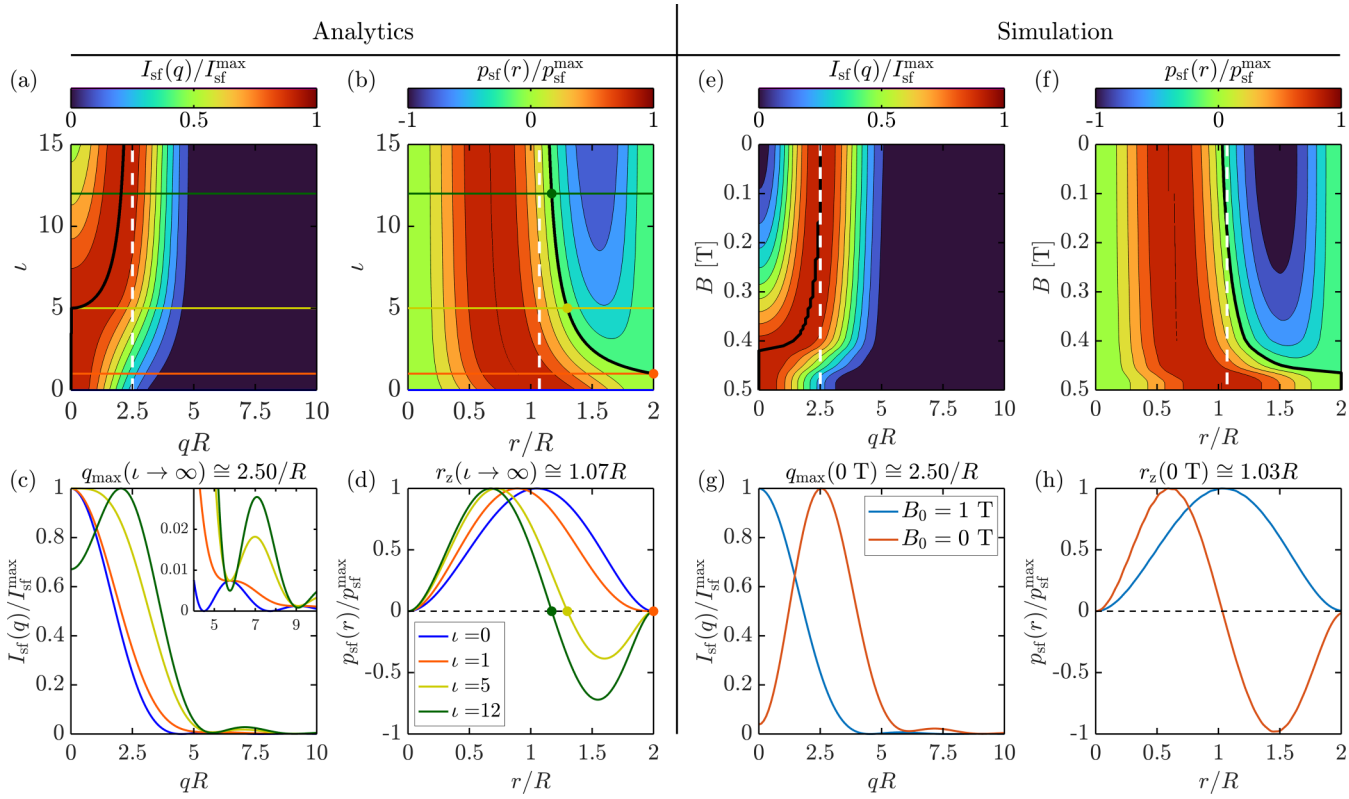

FIG. 1. "Phase diagram" for the azimuthally averaged spin-flip SANS cross section $I_{sf}(q)$ [Eq. (2)] and for the spin-flip pair-distance distribution function $p_{sf}(r)$ [Eq. (3)] within the limits of the first-order magnetization model. The left panel shows the analytical results, while the right panel features the corresponding results of the micromagnetic simulations. The ratio ι of the zero-order coefficient I_{sf}^0 and the first-order coefficient I_{sf}^1 determines the appearance of vortex-type spin structures. Field ($B_0 = \mu_0 H_0$) variations in the simulations correspond to ι variations in the analytical part (zero field: $\iota \to \infty$; saturation: $\iota \to 0$). (a) Color-coded plot of the normalized $I_{sf}(q)$ as a function of $\iota = I_{sf}^1/I_{sf}^0$ and qR. The black solid line in (a) describes the shift of the maximum in $I_{sf}(q)$ towards $q_{max} \cong 2.50/R$ [white dashed line, compare (e)]. (b) Normalized $p_{sf}(r)$ as a function of ι and r/R. The black solid line in (b) describes the shift of the zero in $p_{sf}(r)$ towards $r_z \cong 1.07R$ [white dashed line, compare (f)]. (c) Normalized $I_{sf}(qR)$ and (d) normalized $p_{sf}(r/R)$ for different ι [see the inset in (d)]; the inset in (c) displays $I_{sf}(q)/I_{sf}^{max}$ for $4 < qR < 10$. The colored horizontal lines in (a) and (b) correspond, respectively, to the curves in (c) and (d).

where $\mathbf{r}' = [x', y', z']$ denotes the position vector in the local particle frame. The model consists of 12 expansion coefficients per particle, i.e., three zero-order coefficients m_0^i and nine first-order coefficients m_1^{jk}. For a dilute assembly of spherical nanoparticles, the MNPSE formalism yields the following expression for the azimuthally averaged spin-flip SANS cross section [28,37]:

$$I_{sf}(q) = I_{sf}^0 f(qR)^2 + I_{sf}^1 f'(qR)^2, \tag{2}$$

where R is the particle radius, and the field-dependent coefficients I_{sf}^0 and I_{sf}^1 represent complicated averages of the magnetization coefficients m_0^i and m_1^{jk} over the particle assembly and over the detector plane. The corresponding basis functions are given by ($u = qR$)

$$f(u) = \frac{\sin u - u\cos u}{u^3},$$

$$f'(u) = \frac{df}{du} = \frac{(u^2-3)\sin u + 3u\cos u}{u^4}.$$

Here, $f(u)$ is the form-factor function of the unit sphere [18], and $f'(u)$ is the related first-order derivative. By inverse Fourier transformation, we find from Eq. (2) the related pair-distance distribution function [37]:

$$p_{sf}(r) = I_{sf}^0 \frac{\pi r^2}{6R^3}\left[1 - \frac{3r}{4R} + \frac{r^3}{16R^3}\right] + I_{sf}^1 \frac{\pi r^2}{10R^3}\left[1 - \frac{5r}{4R} + \frac{5r^3}{16R^3} - \frac{r^5}{32R^5}\right]. \tag{3}$$

While the zero-order contribution (I_{sf}^0) arises from symmetric (parallel, positive) correlations only, the first-order contribution (I_{sf}^1) contains antisymmetric (antiparallel, negative) correlations. By comparison to micromagnetic simulations using Mumax3 [41,42]—including isotropic exchange, a random cubic anisotropy [43], the Zeeman interaction, and the demagnetizing field—we find that this linear approach [Eqs. (2) and (3)] already captures the main features of vortex-type spin textures seen in the SANS observables.

The results that are embodied by Eqs. (2) and (3) are summarized in Fig. 1. Prominent features regarding vortex-type spin structures are the decreased spin-flip scattering intensity $I_{sf}(q)$ at momentum transfer $q = 0$ [see Figs. 1(a), 1(c), 1(e), and 1(g)] and the damped oscillatory behavior of the pair-distance distribution function $p_{sf}(r)$ exhibiting negative (antiparallel) correlations related to a vortex [see Figs. 1(b),

1(d), 1(f), and 1(h); compare to [23,31,44]]. In the limiting case of $\iota = I_{\rm sf}^1/I_{\rm sf}^0 \to \infty$ (modeling the remanent state) our linear theory predicts a maximum of $I_{\rm sf}(q)$ at $q_{\rm max} \cong 2.50/R$ [maximum of $[f'(u)]^2$]. This prediction is in excellent agreement with the result from our micromagnetic simulations, where we find $q_{\rm max}(B_0 = 0\ {\rm T}) \cong 2.50/R$ [see Fig. 1(g)]. Furthermore, the relevant zero of $p_{\rm sf}(r)$ is predicted as the result of the following cubic equation that is derived from Eq. (3):

$$\nu^3 + 4\nu^2 + \left(2 - \frac{10}{3\iota}\right)\nu - \left(8 + \frac{40}{3\iota}\right) = 0, \tag{4}$$

where $\nu = r/R$. For $\iota \to \infty$, Eq. (4) predicts the zero at $r_{\rm z} \cong 1.07R$, whereas in our micromagnetic simulations we find $r_{\rm z}(B_0 = 0\ {\rm T}) \cong 1.03R$ [see Fig. 1(h)].

Beyond these limits for the momentum transfer $q_{\rm max}$ and the "zero" correlation length $r_{\rm z}$ we find two specific transition points for ι in the two-dimensional (2D) maps shown in Figs. 1(a) and 1(b). In Fig. 1(b) we observe for $\iota > 1$ the occurrence of negative correlations [negative values of $p_{\rm sf}(r)$], and in Fig. 1(a) we see that the scattering intensity at the origin of reciprocal space, $I_{\rm sf}(q=0)/I_{\rm sf}^{\rm max}$, is constant for $\iota < 5$ and decreases for $\iota > 5$. The micromagnetic simulation results reveal an analogous behavior [compare Figs. 1(e) and 1(f)].

III. MNPSE METHOD: THE CASE OF A LINEAR VORTEX

In the formulation of the linear MNPSE method, the parameters $I_{\rm sf}^0$ and $I_{\rm sf}^1$ [in Eqs. (2) and (3)] are arbitrary functions of the 12 magnetization expansion coefficients in Eq. (1). In the following, we aim to adapt the linear MNPSE method to include physically motivated parameters (replacing $I_{\rm sf}^0$ and $I_{\rm sf}^1$). This approach allows us to obtain a scattering model that is more closely related to the underlying micromagnetic Hamiltonian in the sense that it contains information on the vortex helicity, on the orientation distribution of the vortex axes, and on the transformation behavior of the energies in the Hamiltonian under space inversion.

We consider a dilute assembly of noninteracting spherical nanoparticles that are rigidly embedded in a homogeneous and nonmagnetic matrix. Each particle is assumed to have a random orientation of its (cubic or uniaxial) magnetic anisotropy axis with respect to the externally applied magnetic field $\mathbf{H}_0 \parallel \mathbf{e}_z$, which defines the laboratory frame of reference. In addition to magnetic anisotropy and the Zeeman interaction, we consider an isotropic exchange energy and, most importantly, the magnetodipolar interaction (see the Supplemental Material [37]). When the spin structure of such a spherical nanoparticle is computed starting from saturation, we always find—using the material parameters of iron—a vortex-type texture at low fields and for particle sizes larger than about 20 nm [23,44]. It is the dipolar interaction that is responsible for the vortex formation.

Based on these simulation results, and with the aim to obtain an approximate expression for the spin-flip SANS cross section of an ensemble of vortex-carrying randomly oriented nanoparticles, we introduce a magnetization model with a uniform (constant) part of magnitude m_0 and a linear vortex term of magnitude m_1. More specifically, the basic magnetization vector field is written as

$$\mathbf{M}'(\mathbf{r}') = m_0\mathbf{e}_z' + m_1\mathbf{v}(\mathbf{r}'), \tag{5}$$

where $\mathbf{e}_z' = [0,0,1]$ is the unit vector in the z' direction, $\mathbf{v}(\mathbf{r}') = [-y', x', 0]$ is the linear vortex field, and $\mathbf{r}' = [x', y', z']$ is the position vector with reference to the local vortex frame. Compared to Eq. (1), the number of expansion coefficients in Eq. (5) has been reduced to two. A positive m_1 indicates a counterclockwise (CCW) or right-handed sense of rotation, while a negative m_1 corresponds to a clockwise (CW) or left-handed sense of rotation. We note that for a micromagnetic Hamiltonian that contains the isotropic exchange interaction, magnetic anisotropy, the Zeeman, and magnetodipolar interaction, there exists no preference for CCW or CW vortex rotation senses in the particles. CCW and CW vortices appear with equal probability so that the chiral function averages to zero (see below). However, by including the Dzyaloshinskii-Moriya interaction (DMI), which breaks space-inversion symmetry, chirality selection takes place and leads to a nonzero chiral function [45].

Equation (5) models a linear vortex in the local vortex frame. We introduce a zy rotation matrix $\mathbf{R}(\alpha,\beta)$ that transforms the local magnetization $\mathbf{M}'$ into the laboratory frame of reference, where α and β denote the (global) polar and azimuthal angles, respectively. The resulting global magnetization vector field is then obtained as

$$\mathbf{M}(\mathbf{r};\alpha,\beta) = \mathbf{R}(\alpha,\beta)\cdot\mathbf{M}'(\mathbf{R}^T(\alpha,\beta)\cdot\mathbf{r}). \tag{6}$$

Using Eq. (6) in the MNPSE method [37], we define the ensemble-averaged (dilute) SANS cross sections as

$$\left\langle\frac{d\Sigma_{{\rm sf},\chi}}{d\Omega}\right\rangle = \frac{1}{2}\int_0^{4\pi}\left[\frac{d\Sigma_{{\rm sf},\chi}^{\rm CCW}}{d\Omega} + \frac{d\Sigma_{{\rm sf},\chi}^{\rm CW}}{d\Omega}\right]\psi(\alpha,\beta)d\Upsilon, \tag{7}$$

where $d\Upsilon = \sin\alpha d\alpha d\beta$ is the solid-angle differential, and $\frac{d\Sigma_{{\rm sf},\chi}^{\rm CCW}}{d\Omega}(\mathbf{q};\alpha,\beta)$ and $\frac{d\Sigma_{{\rm sf},\chi}^{\rm CW}}{d\Omega}(\mathbf{q};\alpha,\beta)$ are the SANS cross sections referring to two nanoparticles with the same orientation (α,β), but opposite senses of vortex rotation ($m_1^{\rm CCW} = -m_1^{\rm CW}$). The function $\psi(\alpha,\beta)$ is a field-dependent probability distribution that models the orientation of both the CCW and CW vortex rotation axes (no distinction between the different polarities); its origin is related to the distribution of the net magnetization vectors of the nanoparticles. For simplicity, we assume a uniform distribution $\psi_{\rm u}$ on the spherical surface, which is limited by a field-dependent conical opening angle $0^\circ \leqslant \alpha_{\rm c} \leqslant 90^\circ$. The azimuthally symmetric distribution is then given by (see [37] for details)

$$\psi_{\rm u}(\alpha,\beta) = \frac{\Theta(1-\alpha/\alpha_c)}{2\pi(1-\cos\alpha_{\rm c})}, \tag{8}$$

where $\Theta(\xi)$ is the Heaviside function. In the fully saturated case ($B_0 \to \infty$) it follows that $\alpha_{\rm c} \to 0$, and $\alpha_{\rm c}$ increases with decreasing applied magnetic field. By inserting Eqs. (5)–(8) into the formalism of the MNPSE method, we obtain the following final expressions for the randomly averaged

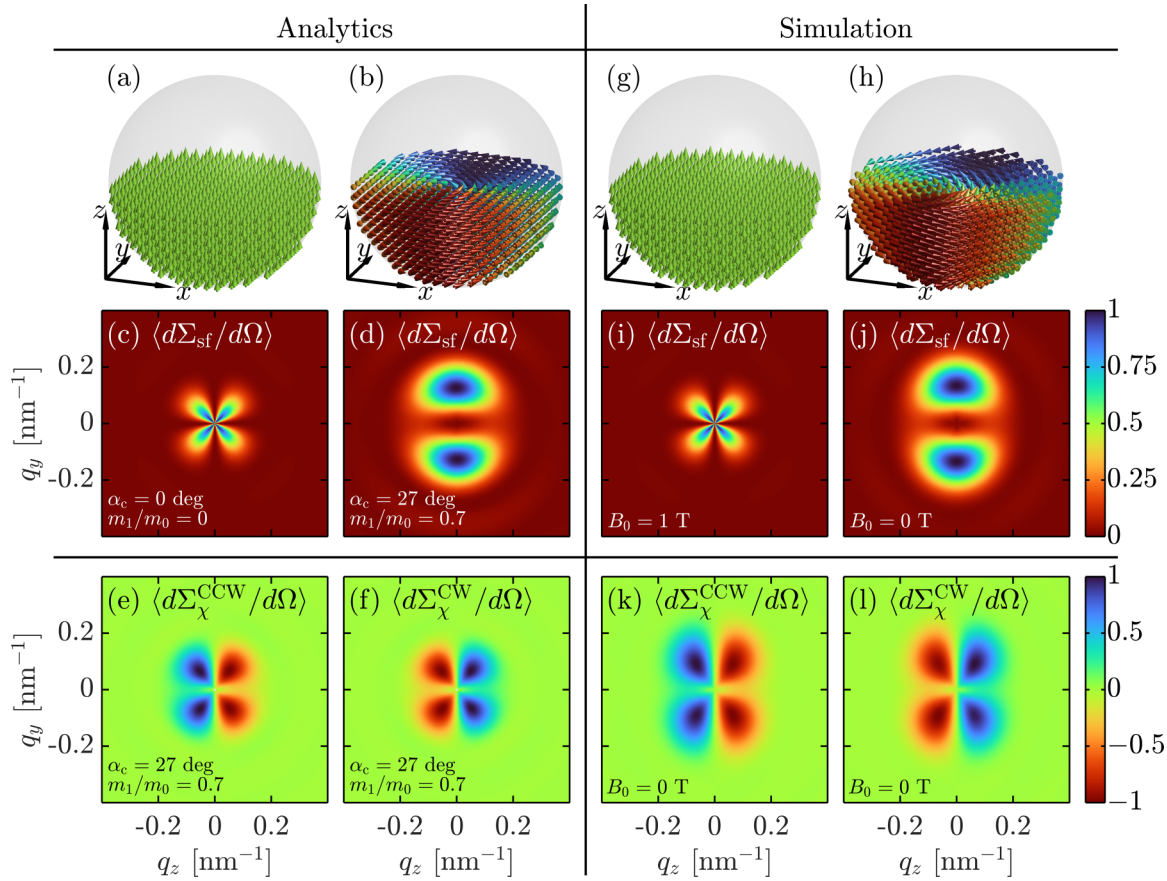

FIG. 2. Illustration of the 2D (normalized) spin-flip SANS cross section and chiral function computed from Eqs. (9) and (10) reflecting the saturation and remanence cases (particle size: $D = 2R = 40$ nm) (linear color scale). Parts (a), (b) and (g), (h) show snapshots of the underlying real-space spin structures. The left panel shows the analytical results, while the right panel features the results of the micromagnetic simulations. The incoming neutron beam ($\parallel \mathbf{e}_x$) is perpendicular to the applied magnetic field $\mathbf{H}_0 \parallel \mathbf{e}_z$ ($B_0 = \mu_0 H_0$). The maximum of the spots in (d) and (j) is found at $q_{y,\max} \cong 2.50/R$. Parts (e), (f) and (k), (l) display the respective chiral functions in the remanent state for counterclockwise (CCW) and clockwise (CW) vortex rotations. Note that the specific values for $\alpha_c = 27^\circ$ and for the ratio $m_1/m_0 = 0.7$ in (d) are based on a fit of the analytical function [Eq. (9)] to the 2D simulation data shown in (j). The value of $\alpha_c = 27^\circ$ corresponds to an applied field of $\sim$0 mT.

2D spin-flip SANS cross section and chiral function [37]:

$$\left\langle \frac{d\Sigma_{\rm sf}}{d\Omega} \right\rangle (q,\theta) = \frac{W}{8}[m_0 f(qR)]^2 \times [12 - (\cos^2\alpha_c + \cos\alpha_c)[3\cos^2(2\theta) + 2\cos(2\theta) + 3] + 4\cos(2\theta)] + \frac{W}{2}[Rm_1 f'(qR)]^2 \times [3 - (2\cos^2\alpha_c + 2\cos\alpha_c - 1)\cos(2\theta)], \tag{9}$$

$$\left\langle \frac{d\Sigma_\chi^{\rm CCW,CW}}{d\Omega} \right\rangle (q,\theta) = \pm W[Rm_0|m_1| f(qR) f'(qR)\cos\theta] \times [4 + \cos^2\alpha_c + \cos\alpha_c - 3(\cos^2\alpha_c + \cos\alpha_c)\cos^2\theta], \tag{10}$$

where W is a scaling constant. In Eq. (10) we have separated the chiral function into CCW ("+" sign) and CW ("−" sign) contributions. For the here-considered micromagnetic energy contributions [37] (with no chirality selection taking place), it then follows that

$$\left\langle \frac{d\Sigma_\chi}{d\Omega} \right\rangle = \frac{1}{2}\left[\left\langle \frac{d\Sigma_\chi^{\rm CCW}}{d\Omega} \right\rangle + \left\langle \frac{d\Sigma_\chi^{\rm CW}}{d\Omega} \right\rangle \right] = 0. \tag{11}$$

Figure 2 displays Eqs. (9) and (10). At saturation [Figs. 2(a) and 2(c) and Figs. 2(g) and 2(i)], with $\alpha_c = 0^\circ$ and $m_1/m_0 = 0$, the spin-flip SANS cross section exhibits the well-known $\sin^2\theta\cos^2\theta$ angular anisotropy. At remanence [Figs. 2(b) and 2(d) and Figs. 2(h) and 2(j)], with $\alpha_c = 27^\circ$ and $m_1/m_0 = 0.7$, we observe for the spin-flip signal an anisotropy that strongly differs from the saturated case, with maxima for $\theta = 90^\circ$. This observation strongly suggests that the magnetization Fourier components are anisotropic, i.e., $\widetilde{M}_{x,y,z} = \widetilde{M}_{x,y,z}(q,\theta)$

[compare to Eq. (4) in [37]]. Consequently, to not lose this information, the experimental data analysis should be concentrated on 2D spin-flip data rather than on the azimuthally averaged 1D data. In micromagnetic simulations of spherical nanoparticles, very similar scattering patterns were observed [27,46].

Averaging Eq. (9) over the angle θ, i.e., $(2\pi)^{-1}\int_0^{2\pi}(\cdots)d\theta$, yields the 1D quantity [37]

$$\langle I_{\rm sf}\rangle(q) = \frac{3W}{16}[m_0 f(qR)]^2(8-3\cos^2\alpha_{\rm c}-3\cos\alpha_{\rm c}) + 8\frac{3W}{16}[m_1 R f'(qR)]^2. \tag{12}$$

By comparison to Eq. (2) we note that the new parameters m_0, m_1, and $\alpha_{\rm c}$ in Eqs. (9) and (10) are related to the coefficient ratio $I^1_{\rm sf}/I^0_{\rm sf}$ as follows:

$$\iota = \frac{I^1_{\rm sf}}{I^0_{\rm sf}} = \frac{8m_1^2R^2}{m_0^2(8-3\cos^2\alpha_{\rm c}-3\cos\alpha_{\rm c})}, \tag{13}$$

which emphasizes the importance of the vortex-axes distribution function. The angle $\alpha_{\rm c}$ may be obtained from the analysis of (preferentially 2D) experimental spin-flip SANS data [compare to Figs. 2(d) and 2(j) and the video clip in [37]].

The here-presented linear vortex model is applicable in cases in which the vortex exhibits a single modulation over the particle radius (with a maximum spin-rotation angle from about 0° to 90° from the center to the surface). For the case of skyrmions, which are expected to form in larger nanoparticles with broken spatial inversion symmetry, a larger rotation angle (by about 180°) may occur so that higher-order terms should be taken into account in the MNPSE expansion. Moreover, as mentioned earlier, we expect the formation of dipolar-energy-driven vortex structures in nanoparticles with a size (diameter) that is significantly larger than the respective single-domain limit [23].

IV. CONCLUSION

In this paper, we have demonstrated that the linear MNPSE approach captures the main effects in the spin-flip SANS cross section and pair-distance distribution function stemming from dilute assemblies of spherical nanoparticles exhibiting vortex-type spin textures. A crucial insight is that the linear functionality represents the most important contribution to the magnetic neutron scattering cross section. Based on the specific case of a linear vortex model, we have derived analytical expressions for the 2D and 1D spin-flip and chiral cross sections of an ensemble of randomly oriented vortex-carrying nanoparticles. The maximum of the spin-flip scattering intensity and the zero of the pair-distance distribution function appear, respectively, at momentum transfer $q_{\rm max} \cong 2.50/R$ and position $r_z \cong 1.07R$, where R denotes the radius of the spherical nanoparticles. The analytical predictions, which enable, e.g., the determination of the field-dependent conical opening angle $\alpha_{\rm c}$ of the vortex-axes distribution from experimental data, are in very good agreement with the results of micromagnetic simulations. The chiral SANS cross section is sensitive to the vortex rotation sense, but in a many-particle system with no chirality selection, it averages to zero (as expected). A candidate for chirality selection is the DMI interaction that breaks space-inversion symmetry.

ACKNOWLEDGMENTS

We acknowledge financial support from the National Research Fund of Luxembourg (AFR Grant No. 15639149, CORE Grant DeQuSky, and PRIDE MASSENA Grant).

[1] M. De, P. S. Ghosh, and V. M. Rotello, Applications of nanoparticles in biology, Adv. Mater. **20**, 4225 (2008).
[2] Y. Diebold and M. Calonge, Applications of nanoparticles in ophthalmology, Prog. Ret. Eye Res. **29**, 596 (2010).
[3] S. C. Baetke, T. Lammers, and F. Kiessling, Applications of nanoparticles for diagnosis and therapy of cancer, Br. J. Radiol. **88**, 20150207 (2015).
[4] W. J. Stark, P. R. Stoessel, W. Wohlleben, and A. Hafner, Industrial applications of nanoparticles, Chem. Soc. Rev. **44**, 5793 (2015).
[5] X. Han, K. Xu, O. Taratula, and F. Khashayar, Applications of nanoparticles in biomedical imaging, Nanoscale **11**, 799 (2019).
[6] A. Lak, S. Disch, and P. Bender, Embracing defects and disorder in magnetic nanoparticles, Adv. Sci. **8**, 2002682 (2021).
[7] X. Batlle, C. Moya, M. Escoda-Torroella, Ò. Iglesias, A. Fraile Rodríguez, and A. Labarta, Magnetic nanoparticles: From the nanostructure to the physical properties, J. Magn. Magn. Mater. **543**, 168594 (2022).
[8] J. A. De Toro, M. Vasilakaki, S. S. Lee, M. S. Andersson, P. S. Normile, N. Yaacoub, P. Murray, E. H. Sánchez, P. Muñiz, D. Peddis, R. Mathieu, K. Liu, J. Geshev, K. N. Trohidou, and J. Nogués, Remanence plots as a probe of spin disorder in magnetic nanoparticles, Chem. Mater. **29**, 8258 (2017).
[9] A. Lappas, G. Antonaropoulos, K. Brintakis, M. Vasilakaki, K. N. Trohidou, V. Iannotti, G. Ausanio, A. Kostopoulou, M. Abeykoon, I. K. Robinson, and E. S. Bozin, Vacancy-driven noncubic local structure and magnetic anisotropy tailoring in Fe_xO-$Fe_{3-\delta}O_4$ nanocrystals, Phys. Rev. X **9**, 041044 (2019).
[10] D. Zákutná, D. Nižňanský, L. C. Barnsley, E. Babcock, Z. Salhi, A. Feoktystov, D. Honecker, and S. Disch, Field dependence of magnetic disorder in nanoparticles, Phys. Rev. X **10**, 031019 (2020).
[11] J. T. Batley, M. Nguyen, I. Kamboj, C. Korostynski, E. S. Aydil, and C. Leighton, Quantitative understanding of superparamagnetic blocking in thoroughly characterized Ni nanoparticle assemblies, Chem. Mater. **32**, 6494 (2020).
[12] C. Kons, M.-H. Phan, H. Srikanth, D. A. Arena, Z. Nemati, J. A. Borchers, and K. L. Krycka, Investigating spin coupling across a three-dimensional interface in core/shell magnetic nanoparticles, Phys. Rev. Mater. **4**, 034408 (2020).
[13] T. Köhler, A. Feoktystov, O. Petracic, E. Kentzinger, T. Bhatnagar-Schöffmann, M. Feygenson, N. Nandakumaran, J. Landers, H. Wende, A. Cervellino, U. Rücker, A. Kovács, R. E.

Dunin-Borkowski, and T. Brückel, Mechanism of magnetization reduction in iron oxide nanoparticles, Nanoscale **13**, 6965 (2021).

[14] Ò. Iglesias and H. Kachkachi, Single nanomagnet behaviour: surface and finite-size effects, in *New Trends in Nanoparticle Magnetism*, edited by D. Peddis, S. Laureti, and D. Fiorani (Springer International, Cham, 2021), pp. 3–38.

[15] E. M. Jefremovas, M. de la Fuente Rodríguez, D. Alba Venero, C. Echevarría-Bonet, P. Bender, B. Fåk, J. A. Blanco, and L. Fernández Barquín, Magnetic super-structure and active surface role in the onset of magnetic excitons revealed in $TbCu_2$ nanoparticles, Commun. Mater. **4**, 56 (2023).

[16] M. Gerina, M. Sanna Angotzi, V. Mameli, V. Gajdošová, D. N. Rainer, M. Dopita, N.-J. Steinke, D. Aurélio, J. Vejpravová, and D. Zákutná, Size dependence of the surface spin disorder and surface anisotropy constant in ferrite nanoparticles, Nanoscale Adv. **5**, 4563 (2023).

[17] S. Mühlbauer, D. Honecker, E. A. Périgo, F. Bergner, S. Disch, A. Heinemann, S. Erokhin, D. Berkov, C. Leighton, M. R. Eskildsen, and A. Michels, Magnetic small-angle neutron scattering, Rev. Mod. Phys. **91**, 015004 (2019).

[18] A. Michels, *Magnetic Small-Angle Neutron Scattering: A Probe for Mesoscale Magnetism Analysis* (Oxford University Press, Oxford, 2021).

[19] K. L. Metlov and A. Michels, Magnetic neutron scattering by magnetic vortices in thin submicron-sized soft ferromagnetic cylinders, Sci. Rep. **6**, 25055 (2016).

[20] A. Michels, D. Mettus, D. Honecker, and K. L. Metlov, Effect of Dzyaloshinski-Moriya interaction on elastic small-angle neutron scattering, Phys. Rev. B **94**, 054424 (2016).

[21] I. Mirebeau, N. Martin, M. Deutsch, L. J. Bannenberg, C. Pappas, G. Chaboussant, R. Cubitt, C. Decorse, and A. O. Leonov, Spin textures induced by quenched disorder in a reentrant spin glass: Vortices versus "frustrated" skyrmions, Phys. Rev. B **98**, 014420 (2018).

[22] A. A. Mistonov, I. S. Dubitskiy, I. S. Shishkin, N. A. Grigoryeva, A. Heinemann, N. A. Sapoletova, G. A. Valkovskiy, and S. V. Grigoriev, Magnetic structure of the inverse opal-like structures: Small angle neutron diffraction and micromagnetic simulations, J. Magn. Magn. Mater. **477**, 99 (2019).

[23] L. G. Vivas, R. Yanes, D. Berkov, S. Erokhin, M. Bersweiler, D. Honecker, P. Bender, and A. Michels, Toward understanding complex spin textures in nanoparticles by magnetic neutron scattering, Phys. Rev. Lett. **125**, 117201 (2020).

[24] V. D. Zaporozhets, Y. Oba, A. Michels, and K. L. Metlov, Small-angle neutron scattering by spatially inhomogeneous ferromagnets with a nonzero average uniaxial anisotropy, J. Appl. Crystallogr. **55**, 592 (2022).

[25] C. Kons, K. L. Krycka, J. Robles, N. Ntallis, M. Pereiro, M.-H. Phan, H. Srikanth, J. A. Borchers, and D. A. Arena, Influence of hard/soft layer ordering on magnetization reversal of bimagnetic nanoparticles: Implications for biomedical/theranostic applications, ACS Appl. Nano Mater. **6**, 10986 (2023).

[26] V. Ukleev, F. Ajejas, A. Devishvili, A. Vorobiev, N.-J. Steinke, R. Cubitt, C. Luo, R.-M. Abrudan, F. Radu, V. Cros, N. Reyren, and J. S. White, Observation by SANS and PNR of pure Néel-type domain wall profiles and skyrmion suppression below room temperature in magnetic $[Pt/CoFeB/Ru]_{10}$ multilayers, STAM Methods **25**, 2315015 (2024).

[27] E. P. Sinaga, M. P. Adams, E. H. Hasdeo, and A. Michels, Neutron-scattering signature of the Dzyaloshinskii-Moriya interaction in nanoparticles, arXiv:2402.00558.

[28] M. P. Adams, E. P. Sinaga, H. Kachkachi, and A. Michels, Signature of surface anisotropy in the spin-flip neutron scattering cross section of spherical nanoparticles: Atomistic simulations and analytical theory, Phys. Rev. B **109**, 024429 (2024).

[29] M. R. Eskildsen, E. M. Forgan, and H. Kawano-Furukawa, Vortex structures, penetration depth and pairing in iron-based superconductors studied by small-angle neutron scattering, Rep. Prog. Phys. **74**, 124504 (2011).

[30] C. Donnelly, K. L. Metlov, V. Scagnoli, M. Guizar-Sicairos, M. Holler, N. S. Bingham, J. Raabe, L. J. Heyderman, N. R. Cooper, and S. Gliga, Experimental observation of vortex rings in a bulk magnet, Nat. Phys. **17**, 316 (2021).

[31] M. Bersweiler, Y. Oba, E. Pratami Sinaga, I. Peral, I. Titov, M. P. Adams, V. Rai, K. L. Metlov, and A. Michels, Fingerprint of vortexlike flux closure in an isotropic Nd-Fe-B bulk magnet, Phys. Rev. B **108**, 094434 (2023).

[32] A. S. Samardak, A. V. Davydenko, A. V. Ognev, Y. S. Jeon, Y. S. Choi, and Y. K. Kim, Size-dependent changeover in magnetization reversal mode of self-assembled one-dimensional chains of spherical Fe_3O_4 nanoparticles, Jpn. J. Appl. Phys. **55**, 100303 (2016).

[33] N. A. Usov, M. S. Nesmeyanov, and V. P. Tarasov, Magnetic vortices as efficient nano heaters in magnetic nanoparticle hyperthermia, Sci. Rep. **8**, 1224 (2018).

[34] G. Niraula, D. Toneto, G. F. Goya, G. Zoppellaro, J. A. H. Coaquira, D. Muraca, J. C. Denardin, T. P. Almeida, M. Knobel, A. I. Ayesh, and S. K. Sharma, Observation of magnetic vortex configuration in non-stoichiometric Fe_3O_4 nanospheres, Nanoscale Adv. **5**, 5015 (2023).

[35] C. Moya, M. Escoda-Torroella, J. Rodríguez-Álvarez, A. I. Figueroa, Í. García, I. B. Ferrer-Vidal, A. Gallo-Cordova, M. Puerto Morales, L. Aballe, A. Fraile Rodríguez, A. Labarta, and X. Batlle, Unveiling the crystal and magnetic texture of iron oxide nanoflowers, Nanoscale **16**, 1942 (2024).

[36] Y. Liu and N. Nagaosa, Current-induced creation of topological vortex rings in a magnetic nanocylinder, Phys. Rev. Lett. **132**, 126701 (2024).

[37] See Supplemental Material at http://link.aps.org/supplemental/10.1103/PhysRevB.110.014420 for further details on the numerical micromagnetic calculations and on the MNPSE method used for the analytical calculation of the spin-flip SANS cross section and chiral function of vortex-carrying nanoparticles. We also provide a video clip that features the field evolution of the spin structure, the 2D and 1D spin-flip SANS cross section, as well as the pair-distance distribution function along the hysteresis loop; the analytical theory is fitted to the 2D numerical SANS results.

[38] M. P. Adams, A. Michels, and H. Kachkachi, Magnetic neutron scattering from spherical nanoparticles with Néel surface anisotropy: atomistic simulations, J. Appl. Crystallogr. **55**, 1488 (2022).

[39] K. L. Krycka, J. A. Borchers, R. A. Booth, S. A. Majetich, Y. Ijiri, K. Hasz, and J. J. Rhyne, Origin of surface canting within Fe_3O_4 nanoparticles, Phys. Rev. Lett. **113**, 147203 (2014).

[40] D. Honecker, A. Ferdinand, F. Döbrich, C. D. Dewhurst, A. Wiedenmann, C. Gómez-Polo, K. Suzuki, and A. Michels, Longitudinal polarization analysis in small-angle neutron scattering, Eur. Phys. J. B **76**, 209 (2010).

[41] A. Vansteenkiste, J. Leliaert, M. Dvornik, M. Helsen, F. Garcia-Sanchez, and B. Van Waeyenberge, The design and verification of MuMax3, AIP Adv. **4**, 107133 (2014).

[42] J. Leliaert, M. Dvornik, J. Mulkers, J. De Clercq, M. V. Milošević, and B. Van Waeyenberge, Fast micromagnetic simulations on GPU-recent advances made with mumax^3, J. Phys. D **51**, 123002 (2018).

[43] In the numerical micromagnetic simulations we use the materials parameters for (cubic) iron, and we also consider the case of a random uniaxial anisotropy (see [37]).

[44] E. Pratami Sinaga, M. P. Adams, M. Bersweiler, L. G. Vivas, E. H. Hasdeo, J. Leliaert, P. Bender, D. Honecker, and A. Michels, Micromagnetic simulation of neutron scattering from spherical nanoparticles: Effect of pore-type defects, Phys. Rev. B **107**, 014416 (2023).

[45] S. V. Maleev, Polarized neutron scattering in magnets, Phys. Usp. **45**, 569 (2002).

[46] M. P. Adams, E. P. Sinaga, and A. Michels, On the angular anisotropy of the randomly averaged magnetic neutron scattering cross section of nanoparticles, IUCrJ **10**, 261 (2023).

Supplemental Material to "Framework for Polarized Magnetic Neutron Scattering from Nanoparticle Assemblies with Vortex-Type Spin Textures"

Michael P. Adams,[1,*] Evelyn Pratami-Sinaga,[1] Štefan Liščák,[1] and Andreas Michels[1,†]

[1] *Department of Physics and Materials Science, University of Luxembourg, 162A Avenue de la Faiencerie, L-1511 Luxembourg, Grand Duchy of Luxembourg*

(Dated: July 1, 2024)

In this Supplemental Material we sketch the main ideas of the multi-nanoparticle power-series expansion (MNPSE) method that is used for the analytical calculation of the spin-flip SANS cross section, the chiral function, and the pair-distance distribution function. Moreover, the main expressions for the polarized SANS cross sections are displayed and details on the numerical micromagnetic simulations are furnished.

I. SCATTERING GEOMETRY AND SPIN-FLIP SANS CROSS SECTION

The quantities of interest in the present paper are the elastic differential spin-flip scattering cross section and the related so-called chiral function, which are usually obtained in an uniaxial polarization-analysis experiment (e.g., [1–5]). For the most commonly used scattering geometry in magnetic SANS experiments (compare Fig. 1), where the applied magnetic field $\mathbf{H}_0 \parallel \mathbf{e}_z$ is perpendicular to the wave vector $\mathbf{k}_0 \parallel \mathbf{e}_x$ of the incident neutrons, the two spin-flip SANS cross sections $d\Sigma_{\rm sf}^{+-}/d\Omega$ and $d\Sigma_{\rm sf}^{-+}/d\Omega$ can be written as [6]:

$$\frac{d\Sigma_{\rm sf}^{+-}}{d\Omega} = \frac{8\pi^3}{V} b_{\rm H}^2 \left(|\widetilde{M}_x|^2 + |\widetilde{M}_y|^2 \cos^4\theta + |\widetilde{M}_z|^2 \sin^2\theta \cos^2\theta - (\widetilde{M}_y \widetilde{M}_z^* + \widetilde{M}_y^* \widetilde{M}_z) \sin\theta \cos^3\theta - i\chi \right), \tag{1}$$

$$\frac{d\Sigma_{\rm sf}^{-+}}{d\Omega} = \frac{8\pi^3}{V} b_{\rm H}^2 \left(|\widetilde{M}_x|^2 + |\widetilde{M}_y|^2 \cos^4\theta + |\widetilde{M}_z|^2 \sin^2\theta \cos^2\theta - (\widetilde{M}_y \widetilde{M}_z^* + \widetilde{M}_y^* \widetilde{M}_z) \sin\theta \cos^3\theta + i\chi \right). \tag{2}$$

The superscripts "+" and "−" refer to the neutron-spin orientation (parallel or antiparallel) relative to the direction of $\mathbf{H}_0$, V denotes the scattering volume, $b_{\rm H} = 2.91 \times 10^8\,{\rm A^{-1}m^{-1}}$ is the magnetic scattering length in the small-angle regime (the atomic magnetic form factor is approximated by 1, since we are dealing with forward scattering), $\widetilde{\mathbf{M}}(\mathbf{q}) = [\widetilde{M}_x(\mathbf{q}), \widetilde{M}_y(\mathbf{q}), \widetilde{M}_z(\mathbf{q})]$ represents the Fourier transform of the magnetization vector field $\mathbf{M}(\mathbf{r}) = [M_x(\mathbf{r}), M_y(\mathbf{r}), M_z(\mathbf{r})]$, θ denotes the angle between $\mathbf{q}$ and $\mathbf{H}_0$, the asterisk "$*$" marks the complex-conjugated quantity, $i^2 = -1$, and $\chi = \chi(\mathbf{q})$ is the chiral function. The latter quantity is obtained from (one-half times) the difference between the two spin-flip SANS cross sections, according to [6]:

$$\begin{aligned} \frac{d\Sigma_\chi}{d\Omega} &= -iK\chi(\mathbf{q}) = \frac{1}{2}\left(\frac{d\Sigma_{\rm sf}^{+-}}{d\Omega} - \frac{d\Sigma_{\rm sf}^{-+}}{d\Omega} \right) \\ &= -iK \left[(\widetilde{M}_x \widetilde{M}_y^* - \widetilde{M}_x^* \widetilde{M}_y) \cos^2\theta - (\widetilde{M}_x \widetilde{M}_z^* - \widetilde{M}_x^* \widetilde{M}_z) \sin\theta \cos\theta \right], \end{aligned} \tag{3}$$

where $K = \frac{8\pi^3}{V} b_{\rm H}^2$. Note that the chiral function vanishes at complete magnetic saturation ($M_x^{H_0 \to \infty} = M_y^{H_0 \to \infty} = 0$) and for purely real-valued or for purely imaginary magnetization Fourier components $\widetilde{M}_{x,y,z}$.

Besides the difference between $d\Sigma_{\rm sf}^{+-}/d\Omega$ and $d\Sigma_{\rm sf}^{-+}/d\Omega$, we can also consider (one-half times) their sum:

$$\begin{aligned} \frac{d\Sigma_{\rm sf}}{d\Omega} &= \frac{1}{2}\left(\frac{d\Sigma_{\rm sf}^{+-}}{d\Omega} + \frac{d\Sigma_{\rm sf}^{-+}}{d\Omega} \right) \\ &= K \left(|\widetilde{M}_x|^2 + |\widetilde{M}_y|^2 \cos^4\theta + |\widetilde{M}_z|^2 \sin^2\theta \cos^2\theta - (\widetilde{M}_y \widetilde{M}_z^* + \widetilde{M}_y^* \widetilde{M}_z) \sin\theta \cos^3\theta \right). \end{aligned} \tag{4}$$

We note that the magnetization Fourier components are in general functions of q and θ, i.e., $\widetilde{M}_{x,y,z} = \widetilde{M}_{x,y,z}(q,\theta)$. The quantity $d\Sigma_{\rm sf}/d\Omega$ is called the (polarization-independent) spin-flip SANS cross section. The following symmetry relations hold for $d\Sigma_{\rm sf}/d\Omega$ (even under spatial inversion of $\mathbf{q}$) and $d\Sigma_\chi/d\Omega$ (odd under spatial inversion of $\mathbf{q}$):

$$\frac{d\Sigma_{\rm sf}}{d\Omega}(\mathbf{q}) = \frac{d\Sigma_{\rm sf}}{d\Omega}(-\mathbf{q}), \tag{5}$$

* Electronic address: michael.adams@uni.lu

† Electronic address: andreas.michels@uni.lu

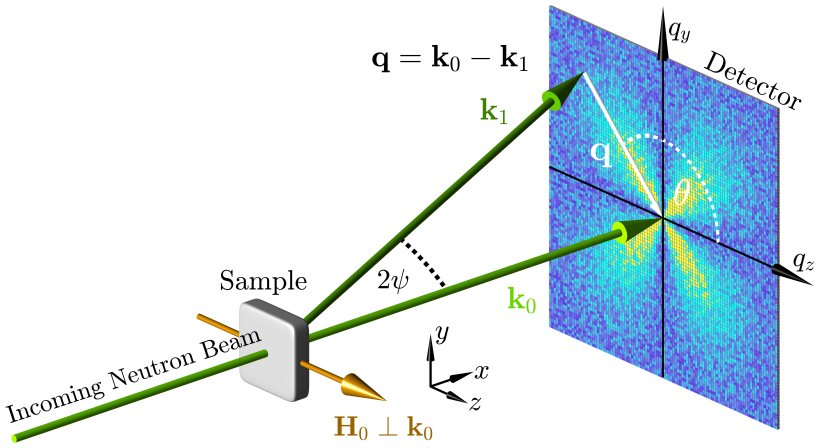

FIG. 1. Sketch of the neutron scattering geometry. The neutron optical elements (polarizer, spin flipper, analyzer) that are required to measure the spin-flip SANS cross section are not drawn. The applied magnetic field $\mathbf{H}_0 \parallel \mathbf{e}_z$ is perpendicular to the wave vector $\mathbf{k}_0 \parallel \mathbf{e}_x$ of the incident neutron beam ($\mathbf{H}_0 \perp \mathbf{k}_0$). The momentum-transfer or scattering vector $\mathbf{q}$ is defined as the difference between $\mathbf{k}_0$ and $\mathbf{k}_1$, i.e., $\mathbf{q} = \mathbf{k}_0 - \mathbf{k}_1$. SANS is usually implemented as elastic scattering ($k_0 = k_1 = 2\pi/\lambda$), and the component of $\mathbf{q}$ along the incident neutron beam, here q_x, is much smaller than the other two components so that $\mathbf{q} \cong [0, q_y, q_z] = q[0, \sin\theta, \cos\theta]$. This demonstrates that SANS probes predominantly correlations in the plane perpendicular to the incident beam. For elastic scattering, the magnitude of $\mathbf{q}$ is given by $q = (4\pi/\lambda)\sin(\psi)$, where λ denotes the mean wavelength of the neutrons and 2ψ is the scattering angle. The angle $\theta = \angle(\mathbf{q}, \mathbf{H}_0)$ is used to describe the angular anisotropy of the recorded scattering pattern on the two-dimensional position-sensitive detector.

$$\frac{d\Sigma_\chi}{d\Omega}(\mathbf{q}) = -\frac{d\Sigma_\chi}{d\Omega}(-\mathbf{q}). \tag{6}$$

It is often convenient to average two-dimensional SANS data $f(\mathbf{q}) = f(q_y, q_z) = f(q, \theta)$, where f either stands for $d\Sigma_{\rm sf}/d\Omega$ or for $d\Sigma_\chi/d\Omega$, along certain directions in $\mathbf{q}$ space, e.g. parallel ($\theta = 0$) or perpendicular ($\theta = \pi/2$) to the applied magnetic field, or even over the full angular θ range. In this paper, we consider 2π azimuthally-averaged SANS data

$$I_{\rm sf}(q) = \frac{1}{2\pi}\int_0^{2\pi} f(q,\theta)\, d\theta, \tag{7}$$

which allows for the computation of the pair-distance distribution function $p_{\rm sf}(r)$ according to

$$p_{\rm sf}(r) = r\int_0^\infty I_{\rm sf}(q)\sin(qr) q dq. \tag{8}$$

This Fourier transform corresponds to the distribution of real-space distances between volume elements inside the particle weighted by the excess scattering-length density distribution. As a reference for nonuniformly magnetized spherical particles, we specify here the $p_{\rm sf}(r)$ of a uniformly magnetized sphere, which for $r \le D = 2R$ equals:

$$p_{\rm sf}(r) \propto r^2\left(1 - \frac{3r}{4R} + \frac{r^3}{16R^3}\right). \tag{9}$$

For the calculation of the spin-flip SANS cross section $d\Sigma_{\rm sf}/d\Omega$ [Eq. (4)] and the chiral function $d\Sigma_\chi/d\Omega$ [Eq. (3)], it is necessary to compute the discrete Fourier transform of all the $\mathbf{m}_i = \mathbf{m}_i(\mathbf{r})$ belonging to the spherical nanomagnet. Using $\boldsymbol{\mu}_i = \boldsymbol{\mu}_i(\mathbf{r}) = M_{\rm s} V_i \mathbf{m}_i(\mathbf{r})$, the discrete-space Fourier transform is computed as ($V_i = a^3$):

$$\widetilde{\mathbf{M}}(\mathbf{q}) \cong \frac{M_{\rm s} a^3 h(\mathbf{q})}{(2\pi)^{3/2}} \sum_{i=1}^{\mathcal{K}} \mathbf{m}_i \exp\left(-\mathrm{i}\mathbf{q}\cdot\mathbf{r}_i\right), \tag{10}$$

where $\mathbf{r}_i$ is the location point of the ith spin and $\mathbf{q}$ represents the wave vector (scattering vector). The function

$$h(\mathbf{q}) = \frac{\sin(q_x a/2)}{q_x a/2}\frac{\sin(q_y a/2)}{q_y a/2}\frac{\sin(q_z a/2)}{q_z a/2} \tag{11}$$

denotes the form factor of the cubic discretization cell with $a = 2\,\mathrm{nm}$ being the cell size; for $|q_{x,y,z}|a/2 \ll 1$, $h \to 1$. For atomistic calculation [7, 8], this correction is irrelevant in the small-angle regime, but for the present calculation, the cell size becomes already noticeable for $q \gtrsim 0.3\,\mathrm{nm}^{-1}$. Equation (10) establishes the relation between the outcome of the simulations, $\mathbf{m}_i$, and $d\Sigma_{\mathrm{sf}}/d\Omega$ and $d\Sigma_{\chi}/d\Omega$. The Fourier components are evaluated in the plane $q_x = 0$ (corresponding to the scattering geometry shown in Fig. 1 with $\mathbf{q} \cong [0, q_y, q_z] = q[0, \sin\theta, \cos\theta]$) and used in Eqs. (3) and (4) to compute the spin-flip SANS cross section and the chiral function.

II. DETAILS ON THE MICROMAGNETIC SIMULATIONS

We were using the open-source software package Mumax3 (version 3.10) for the micromagnetic simulations [9, 10]. This program is a widely used micromagnetic simulation tool that enables researchers to investigate the static and dynamic nanoscale behavior of magnetic materials. Mumax3 employs a finite-difference discretization scheme of space using an orthorhombic grid of cells. The following contributions to the total magnetic Gibbs free energy $G = E_{\mathrm{z}} + E_{\mathrm{d}} + E_{\mathrm{ani}} + E_{\mathrm{ex}}$ were taken into account: Zeeman energy E_{z} in the external magnetic field, dipolar (magnetostatic) interaction energy E_{d}, energy of the (cubic) magnetocrystalline anisotropy E_{ani}, and the isotropic and symmetric exchange energy E_{ex}. The continuum expressions for these energies are the following [11]:

$$E_{\mathrm{z}} = -\mu_0 M_{\mathrm{s}} \int \mathbf{m} \cdot \mathbf{H}_0 \, dV, \tag{12}$$

$$E_{\mathrm{d}} = -\frac{1}{2}\mu_0 M_{\mathrm{s}} \int \mathbf{m} \cdot \mathbf{H}_{\mathrm{d}} \, dV, \tag{13}$$

$$E_{\mathrm{ani}} = K_{\mathrm{c1}} \int \left[(\mathbf{c}_1 \cdot \mathbf{m})^2 (\mathbf{c}_2 \cdot \mathbf{m})^2 + (\mathbf{c}_1 \cdot \mathbf{m})^2 (\mathbf{c}_3 \cdot \mathbf{m})^2 + (\mathbf{c}_2 \cdot \mathbf{m})^2 (\mathbf{c}_3 \cdot \mathbf{m})^2 \right] dV, \tag{14}$$

$$E_{\mathrm{ex}} = A \int \left[(\nabla m_x)^2 + (\nabla m_y)^2 + (\nabla m_z)^2 \right] \, dV, \tag{15}$$

where $\mu_0 = 4\pi \times 10^{-7}\,\mathrm{Tm/A}$, $\mathbf{m}(\mathbf{r}) = \mathbf{M}(\mathbf{r})/M_{\mathrm{s}}$ denotes the unit magnetization vector field with M_{s} being the saturation magnetization, $\mathbf{H}_0$ is the (constant) applied magnetic field, $\mathbf{H}_{\mathrm{d}} = \mathbf{H}_{\mathrm{d}}(\mathbf{r}; \mathbf{M}(\mathbf{r}))$ is the magnetostatic self-interaction field, K_{c1} is the first-order cubic anisotropy constant with the $\mathbf{c}_{1,2,3}$ vectors representing the local (mutually perpendicular) cubic anisotropy axes [12], A is the exchange-stiffness constant, and the integrals are taken over the volume of the sample. In the simulations, we used the following material parameters for iron: $M_{\mathrm{s}} = 1700\,\mathrm{kA/m}$, $K_{\mathrm{c1}} = +4.7 \times 10^4\,\mathrm{J/m^3}$, and $A = 1.0 \times 10^{-11}\,\mathrm{J/m}$. These values result in a magnetostatic exchange length of $l_{\mathrm{s}} = \sqrt{2A/(\mu_0 M_{\mathrm{s}}^2)} = 2.3\,\mathrm{nm}$ and in a domain-wall parameter of $l_{\mathrm{k}} = \sqrt{A/K_{\mathrm{c1}}} = 14.6\,\mathrm{nm}$. We refer to Ref. [9] for a discussion of how the above continuum expressions for the magnetic energies are numerically implemented on a discrete spatial grid.

We carried out simulations for a sphere diameter of $D = 40\,\mathrm{nm}$. The sphere volume was discretized into cubical cells "i" with a size (volume) of $V_i = 2 \times 2 \times 2\ \mathrm{nm}^3$ (finite-difference method). This cell size is motivated by the above values for l_{s} and l_{k} and by the aim to resolve spatial variations in the magnetization that are smaller than these characteristic length scales. In each cell "i" with volume V_i, the magnetic moment vector is given by $\boldsymbol{\mu}_i = \boldsymbol{\mu}_i(\mathbf{r}) = M_{\mathrm{s}} V_i \mathbf{m}_i(\mathbf{r})$, where $\mathbf{m}_i(\mathbf{r})$ is a unit vector along the local direction of the magnetization. Open boundary conditions were used. We are interested in the scattering behavior of an ensemble of noninteracting particles having random easy-axis orientations; 800 random orientations between the cubic anisotropy axes and $\mathbf{H}_0$ were used to compute randomly-averaged quantities. All simulations were carried out by first saturating the nanoparticle by a strong external field $\mathbf{H}_0$, and then the field was decreased in steps of typically 5 mT following the major hysteresis loop. For each step of H_0 and for each particular easy-axis orientation, we have obtained the equilibrium spin structure $m_{x,y,z}(x, y, z)$ by employing both the "Relax" and "Minimize" functions of Mumax3. The former solves the Landau-Lifshitz-Gilbert equation without the precessional term and the latter uses the conjugate-gradient method to find the configuration of minimum energy.

Using the results of the Mumax3 simulations, we determine the vortex rotation axis vector $\mathbf{a}$ of a particular magnetization structure by employing a linear least-squares method. For this analysis, we assume the following linear magnetization function:

$$\mathbf{m}_{\mathrm{lin}}(\mathbf{r}) = \begin{bmatrix} m_0^x \\ m_0^y \\ m_0^z \end{bmatrix} + \begin{bmatrix} m_1^{xx} & m_1^{xy} & m_1^{xz} \\ m_1^{yx} & m_1^{yy} & m_1^{yz} \\ m_1^{zx} & m_1^{zy} & m_1^{zz} \end{bmatrix} \cdot \begin{bmatrix} x \\ y \\ z \end{bmatrix}, \tag{16}$$

and minimize the following mean-square-error function:

$$\epsilon = \frac{1}{n}\sum_{k=1}^{n} \|\mathbf{m}_k - \mathbf{m}_{\rm lin}(\mathbf{r}_k)\|^2, \tag{17}$$

where $\mathbf{m}_k$ is the magnetization vector of the simulation cell "k", $\mathbf{r}_k$ is the corresponding position vector, and n denotes the number of discretization cells of an individual particle. The minimization of ϵ is achieved by solving the following system of linear equations (with $\kappa \in \{x, y, z\}$):

$$\mathbf{A}\mathbf{x}_\kappa = \mathbf{v}_\kappa, \tag{18}$$

with the system matrix

$$\mathbf{A} = \sum_{k=1}^{n} \begin{bmatrix} 1 & \mathbf{r}_k^T \\ \mathbf{r}_k & \mathbf{r}_k \otimes \mathbf{r}_k \end{bmatrix}, \tag{19}$$

the coefficient vector

$$\mathbf{x}_\kappa = \begin{bmatrix} m_0^\kappa & m_1^{\kappa x} & m_1^{\kappa y} & m_1^{\kappa z} \end{bmatrix}^T, \tag{20}$$

and the constant vector

$$\mathbf{v}_\kappa = \sum_{k=1}^{n} \begin{bmatrix} m_k^\kappa \\ m_k^\kappa \mathbf{r}_k \end{bmatrix}. \tag{21}$$

The normalized rotation axis vector $\mathbf{a}$ is then computed from the curl of the linear magnetization function [Eq. (16)] as follows

$$\mathbf{a} = \frac{\nabla \times \mathbf{m}_{\rm lin}}{\|\nabla \times \mathbf{m}_{\rm lin}\|} = \frac{[m_1^{zy} - m_1^{yz},\ m_1^{xz} - m_1^{zx},\ m_1^{yx} - m_1^{xy}]}{\sqrt{(m_1^{zy} - m_1^{yz})^2 + (m_1^{xz} - m_1^{zx})^2 + (m_1^{yx} - m_1^{xy})^2}}. \tag{22}$$

In the fully saturated state, the vector $\mathbf{a}$ does not exist since the magnetization is uniform.

Figure 2 displays micromagnetic simulation data for the vortex profile in the remanent state. It is seen that the radial component m_ρ is equal to zero over the particle radius (on the average), while the tangential component m_β increases to unity (due to flux closure), and the magnetization component m_z decreases from about unity at the sphere center to a slightly negative but constant value at the radius. Figure 8 shows the corresponding results for a uniaxial particle anisotropy (Fig. 2 is for a cubic particle anisotropy).

The vortex-axes distribution function $\psi(\alpha, \beta)$, for use in Eq. (74) to compute the spin-flip SANS cross section and chiral function, is extracted from the Mumax3 simulation data using the following recipe: (i) We assume a given set of nonzero random vectors $\mathbf{m}^k = [m_x^k, m_y^k, m_z^k]$ with $k = \{1, 2, 3, ..., K\}$. These random vectors are represented by either the easy axes of the particles, their net magnetizations, or their vortex axes [see Fig. 3(a,b,c)]. (ii) We compute the corresponding set of spherical angles

$$\alpha^k = \arctan2\left(\sqrt{(m_x^k)^2 + (m_y^k)^2}, m_z^k\right), \tag{23}$$

$$\beta^k = \arctan2\left(m_y^k, m_x^k\right), \tag{24}$$

which are plotted in Fig. 3(d,e,f). (iii) We define a rectangular grid

$$\alpha_\mu = h\mu + h/2, \qquad \mu = \{0, 1, 2, ..., N-1\}, \tag{25}$$

$$\beta_\nu = h\nu + h/2, \qquad \nu = \{0, 1, 2, ..., 2N-1\}, \tag{26}$$

where $h = \pi/N$ is the step size (the grid consists of $N \times 2N$ squares of side length h, where the (α_μ, β_ν) are the center points of the squares). (iv) From the data set (α^k, β^k) we compute the empirical probability $P_{\mu\nu}$ corresponding to the binning (α_μ, β_ν):

$$P_{\mu\nu} = \frac{1}{K}\sum_{k=1}^{K} \delta_{\mu\nu}(\alpha^k, \beta^k), \tag{27}$$

$$\delta_{\mu\nu}(\alpha^k, \beta^k) = \begin{cases} 1 & , \text{ if } (-h/2 < \alpha^k - \alpha_\mu < h/2) \wedge (-h/2 < \beta^k - \beta_\nu < h/2) \\ 0 & , \text{ else} \end{cases}. \tag{28}$$

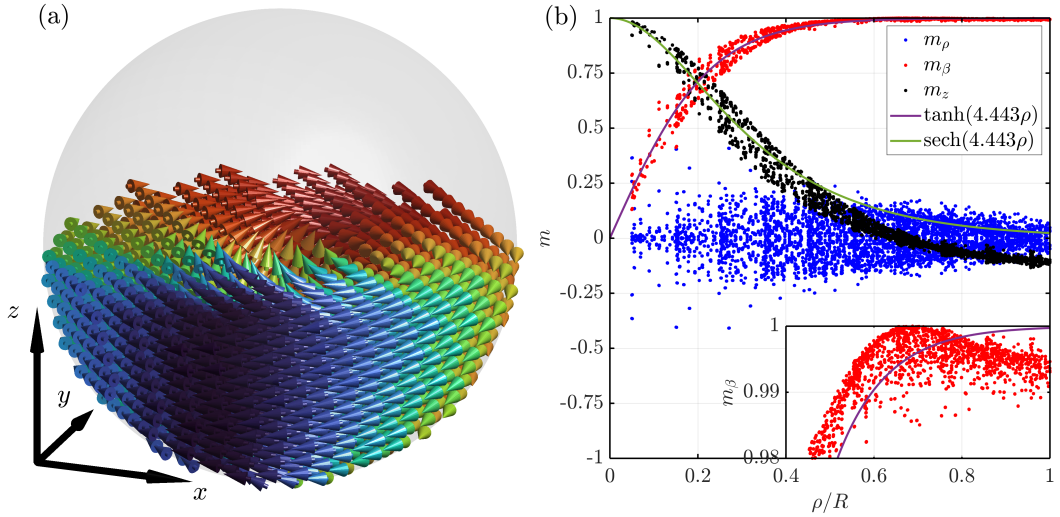

FIG. 2. (a) Example for a real-space spin structure in the remanent state ($B_0 = 0\,\mathrm{T}$). (b) Vortex profile in the remanent state. The data points represent the collective magnetization data of 10 nanoparticles with 4224 magnetic moments each with reference to their individual vortex reference frame. The orientation of the cubic anisotropy varies randomly from particle to particle (particle size is 40 nm, discretized into $2 \times 2 \times 2$ nm^3). Initially all structures were saturated by a strong applied field $\mathbf{H}_0 \parallel \mathbf{e}_z$. The cylindrical components of the magnetization, m_ρ, m_β, m_z, are represented as a function of the cylinder radius $\rho = \sqrt{x^2+y^2}$ and follow the constraint that $m_\rho^2 + m_\beta^2 + m_z^2 = 1$. The azimuthal component m_β and the axial component m_z approximately follow hyperbolic tangent and secant functions, respectively.

The summation over the $P_{\mu\nu}$ is equal to unity:

$$\sum_{\mu=0}^{N-1} \sum_{\nu=0}^{2N-1} P_{\mu\nu} = 1. \tag{29}$$

(v) By normalizing the empirical probability, we estimate the spherical probability distribution $\psi_{\mu\nu}$ as follows:

$$\psi(\alpha_\mu, \beta_\nu) \approx \psi_{\mu\nu} = \frac{P_{\mu\nu}}{h^2 \sin(\alpha_\mu)}, \qquad \left[\text{spherical normalization } \int_0^{2\pi}\int_0^{\pi} \psi(\alpha,\beta)\sin\alpha\, d\alpha d\beta = 1\right]. \tag{30}$$

(vi) By assuming azimuthal symmetry, we can improve the statistics by averaging (integration using the trapezoidal rule) and rescaling by the factor $(2\pi)^{-1}$:

$$\psi(\alpha,\beta) \approx \psi_\mu = \frac{1}{2\pi}\frac{h}{2}\sum_{\nu=0}^{2N-2}(\psi_{\mu,\nu} + \psi_{\mu,\nu+1}), \qquad \left[\text{azimuthal symmetry: } \psi(\alpha,\beta) = \frac{1}{2\pi}\int_0^{2\pi}\psi(\alpha,\beta)d\beta\right] \tag{31}$$

(vii) The resulting numbers ψ_μ are displayed in Fig. 3(g,h,i). In Fig. 3(g) we show that, for the case of a uniform distribution on the spherical surface, the probability distribution function $\psi(\alpha,\beta) = (4\pi)^{-1}$. This result is reasonable due to the spherical normalization foe the probability distribution function ψ.

III. MULTI-NANOPARTICLE POWER-SERIES EXPANSION (MNPSE) METHOD FOR THE POLARIZED SANS CROSS SECTION

For the sake of self-contained presentation, we repeat here the main steps of the MNPSE approach [8].

A. Magnetization power-series expansion, Fourier cross-correlation matrix, and spin-flip SANS cross section

We consider an ensemble of magnetic nanoparticles rigidly embedded in a nonmagnetic and homogeneous matrix. The global magnetization vector field of the system, $\mathbf{M}(\mathbf{r}) = [M^x(\mathbf{r}), M^y(\mathbf{r}), M^z(\mathbf{r})]$, is generally a discontinuous

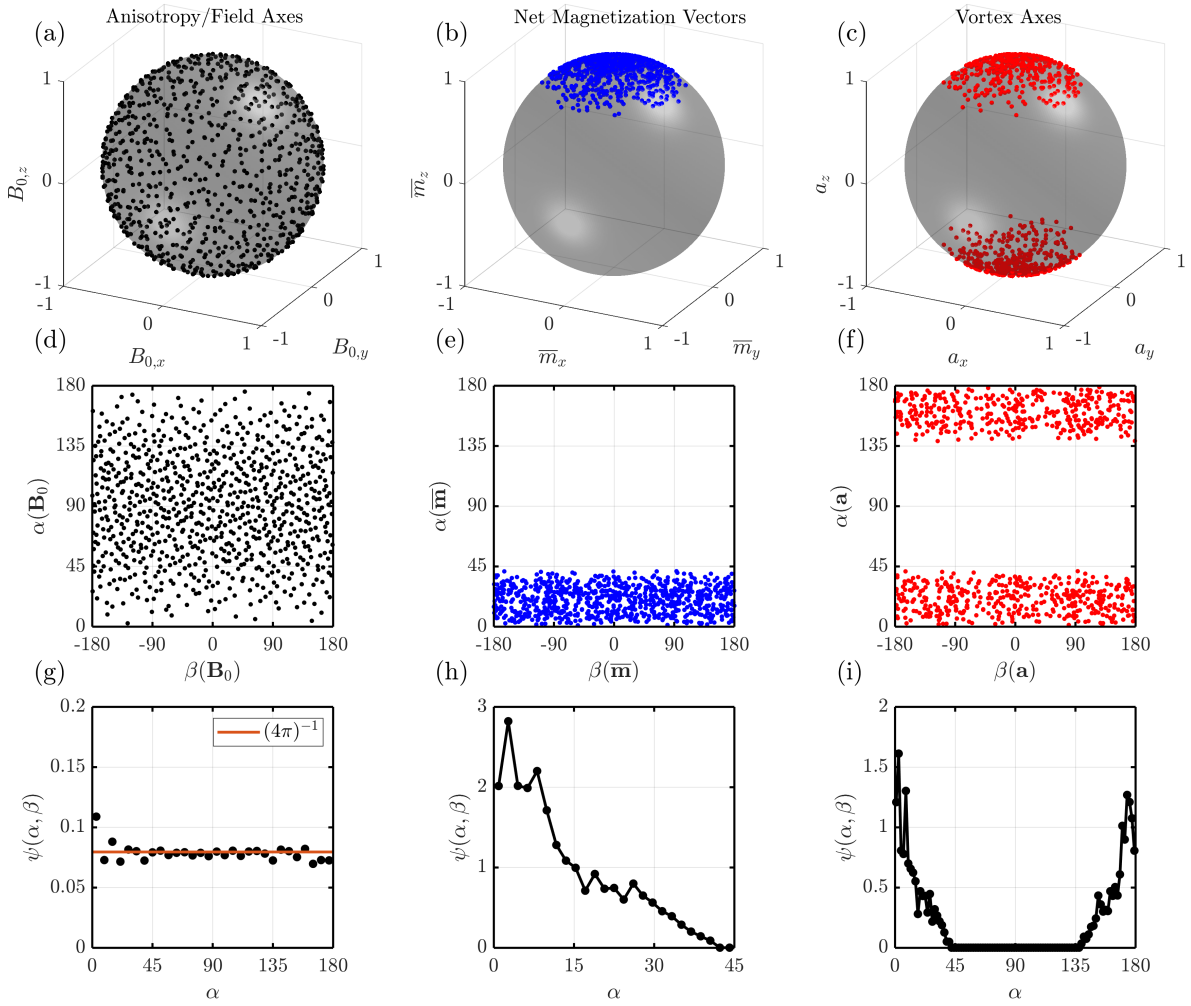

FIG. 3. Distribution of (a) the cubic anisotropy axes/applied fields, (b) the net (average) magnetization vectors, and (c) the vortex rotation axes vectors on the unit sphere at remanence. Initially all structures were saturated by a strong applied field $\mathbf{H}_0 \parallel \mathbf{e}_z$. Data of 800 particles with random cubic anisotropy are shown. α and β in (d,e,f) denote the respective polar and azimuthal angles [computed according to Eqs. (23) and (24)]. The anisotropy axes are randomly distributed over the whole unit sphere and follow a $\psi(\alpha,\beta) = (4\pi)^{-1}$ distribution function (g). The net magnetization vectors at remanence, $\overline{\mathbf{m}}$, are azimuthally-symmetric (β independent) and bound by $\alpha \lesssim 45°$ (h). The uniaxial vortex rotation axes $\mathbf{a}$ are symmetrically bound by $0° \lesssim \alpha \lesssim 45°$ and $135° \lesssim \alpha \lesssim 180°$ and (for $\alpha \lesssim \alpha_c = 45°$) approximately follow a $\psi(\alpha,\beta) = \Theta(1-\alpha/\alpha_c)/[2\pi(1-\cos\alpha_c)]$ distribution (i). The vortex axes in the upper hemisphere ($\alpha < 90°$) correspond to a mathematically positive rotation in the xy plane and vice versa for the lower hemisphere ($\alpha > 90°$).

function, since $\mathbf{M}$ vanishes in the space between the particles; $\mathbf{r} = [x, y, z]$ is the position vector in the laboratory frame. For the formulation of this discontinuous behavior, we use the indicator function (or particle shape function with particle index ν)

$$S_\nu(\mathbf{r}'_\nu) = \begin{cases} 1 & , \mathbf{r}'_\nu \in V'_\nu \\ 0 & , \mathbf{r}'_\nu \notin V'_\nu \end{cases}, \tag{32}$$

where $V'_\nu \subset \mathbb{R}^3$ denotes the set of points within the ν-th particle volume with reference to the local particle frame, and $\mathbf{r}'_\nu = [x'_\nu, y'_\nu, z'_\nu]$ represent the local coordinates (see Fig. 4). The transformation between the global point set V_ν and the local point set V'_ν is then obtained by $V'_\nu = \{\mathbf{r} - \mathbf{a}_\nu : \mathbf{r} \in V_\nu\}$ (with the inverse transformation: $V_\nu = \{\mathbf{r}'_\nu + \mathbf{a}_\nu : \mathbf{r}'_\nu \in V'_\nu\}$), where $\mathbf{a}_\nu = [a^x_\nu, a^y_\nu, a^z_\nu]$ is a constant shift vector that points from the origin of the global $\mathbf{r}$ coordinate system to the origin of the local $\mathbf{r}'_\nu$ system. The corresponding linear coordinate transformation is then given by $\mathbf{r}'_\nu = \mathbf{r} - \mathbf{a}_\nu$, while the volume v_ν of the ν-th particle is obtained via integration of the corresponding shape

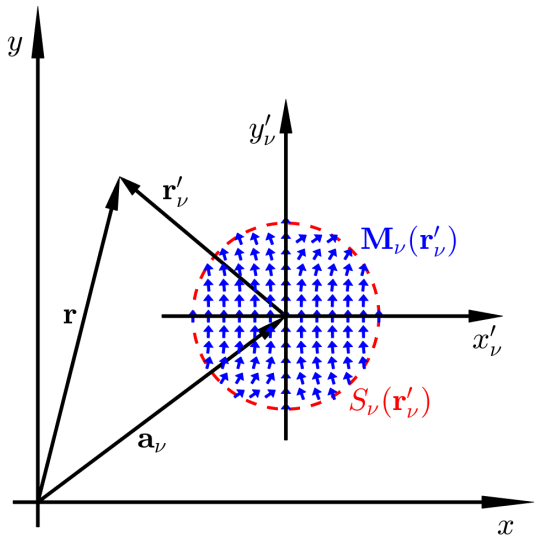

FIG. 4. Sketch illustrating the relationship between the global unprimed ($\mathbf{r}$) laboratory coordinate system and the local primed ($\mathbf{r}'_\nu$) system of particle ν with magnetization $\mathbf{M}_\nu(\mathbf{r}'_\nu)$ and shape function $S_\nu(\mathbf{r}'_\nu)$. $\mathbf{a}_\nu$ is a constant shift vector that points from the origin of the global $\mathbf{r}$ coordinate system to the origin of the local $\mathbf{r}'_\nu$ system. For simplicity, the z coordinate specifying the third space dimension has been ignored.

function:

$$v_\nu = \int_{\mathbb{R}^3} S_\nu(\mathbf{r}'_\nu) d^3 r'_\nu. \tag{33}$$

To account for an inhomogeneous magnetic microstructure, we describe the Cartesian magnetization vector field components M^μ_ν (with $\mu \in \{x, y, z\}$) for the ν-th particle as the product of its shape function and a power series:

$$M^\mu_\nu(\mathbf{r}'_\nu) = S_\nu(\mathbf{r}'_\nu) \sum_{k,m,n=0}^{\infty} M^\mu_{\nu,(k,m,n)} x'^k_\nu y'^m_\nu z'^n_\nu, \tag{34}$$

where $M^\mu_{\nu,(k,m,n)}$ are arbitrary constant expansion coefficients, which may depend on temperature, applied magnetic field, and the type of material. The global Cartesian magnetization vector field components M^μ then follow as the sum over the individual magnetization components M^μ_ν shifted by $\mathbf{a}_\nu$:

$$\begin{aligned} M^\mu(\mathbf{r}) &= \sum_{\nu=1}^{\mathcal{K}} M^\mu_\nu(\mathbf{r} - \mathbf{a}_\nu) \\ &= \sum_{\nu=1}^{\mathcal{K}} \left[S_\nu(\mathbf{r} - \mathbf{a}_\nu) \sum_{k,m,n=0}^{\infty} M^\mu_{\nu,(k,m,n)} (x - a^x_\nu)^k (y - a^y_\nu)^m (z - a^z_\nu)^n \right], \end{aligned} \tag{35}$$

$\mathcal{K}$ being the number of particles in the assembly. For the further derivations, we prefer the Einstein and multi-index notation. Using these notation concepts, Eq. (35) reads:

$$M^\mu(\mathbf{r}) = S_\nu(\mathbf{r} - \mathbf{a}_\nu) M^\mu_{\nu,\boldsymbol{\alpha}} (\mathbf{r} - \mathbf{a}_\nu)^{\boldsymbol{\alpha}}, \tag{36}$$

where $\boldsymbol{\alpha} = (k, m, n)$ represents a multi-index. The zero-order case of $\boldsymbol{\alpha} = (0, 0, 0)$ corresponds to the situation of an ensemble of uniformly magnetized nanoparticles. Higher-order terms in this series take into account the local spatial nonuniformities in $\mathbf{M}$.

For the computation of the magnetic SANS cross section, the next step is to perform the spatial Fourier transform

$$\widetilde{M}^\mu(\mathbf{q}) = \frac{1}{(2\pi)^{3/2}} \int_{\mathbb{R}^3} M^\mu(\mathbf{r}) \exp(-i\mathbf{q} \cdot \mathbf{r}) d^3 r. \tag{37}$$

Instead of direct integration, we can use the shift and derivation theorem of Fourier theory, such that the Fourier transform of Eq. (36) can be expressed as

$$\widetilde{M}^{\mu}(\mathbf{q}) = i^{|\boldsymbol{\alpha}|} M^{\mu}_{\nu,\boldsymbol{\alpha}} \exp(-\mathrm{i}\mathbf{q}\cdot\mathbf{a}_{\nu}) \partial^{\boldsymbol{\alpha}} \widetilde{S}_{\nu}(\mathbf{q}), \tag{38}$$

where i is the imaginary number ($i^2 = -1$).

In the sequel, the derivative $\partial^{\boldsymbol{\alpha}}$, with $\boldsymbol{\alpha} = (k, m, n)$, will denote the $|\boldsymbol{\alpha}|$-th order mixed partial derivative

$$\partial^{\boldsymbol{\alpha}} \equiv \frac{\partial^k}{\partial q_x^k} \frac{\partial^m}{\partial q_y^m} \frac{\partial^n}{\partial q_z^n}, \tag{39}$$

with $|\boldsymbol{\alpha}| = k + m + n$ being the sum of components of the multi-index $\boldsymbol{\alpha} = (k, m, n)$. Likewise, the compact sum $\sum_{\boldsymbol{\alpha}}$ should be understood as the triple sum $\sum_k \sum_m \sum_n$. $\widetilde{S}_{\nu}(\mathbf{q})$ is the Fourier transform of the indicator function defined by

$$\widetilde{S}_{\nu}(\mathbf{q}) = \frac{1}{(2\pi)^{3/2}} \int_{\mathbb{R}^3} S_{\nu}(\mathbf{r}) \exp(-\mathrm{i}\mathbf{q}\cdot\mathbf{r}) d^3 r. \tag{40}$$

Next, introducing the following Fourier cross-correlation functions $\widetilde{\Gamma}^{\iota\kappa} : \mathbb{R}^3 \to \mathbb{C}$ with $\iota, \kappa \in \{x, y, z\}$ ("$*$" stands for the complex conjugate),

$$\begin{aligned} \widetilde{\Gamma}^{\iota\kappa}(\mathbf{q}) &= \left[\widetilde{M}^{\iota}(\mathbf{q})\right] \left[\widetilde{M}^{\kappa}(\mathbf{q})\right]^{*} \\ &= i^{|\boldsymbol{\alpha}|-|\boldsymbol{\beta}|} M^{\iota}_{\nu,\boldsymbol{\alpha}} M^{\kappa}_{\mu,\boldsymbol{\beta}} \exp(-\mathrm{i}\mathbf{q}\cdot[\mathbf{a}_{\nu} - \mathbf{a}_{\mu}]) \partial^{\boldsymbol{\alpha}} \widetilde{S}_{\nu}(\mathbf{q}) \partial^{\boldsymbol{\beta}} \widetilde{S}^{*}_{\mu}(\mathbf{q}), \end{aligned} \tag{41}$$

we rewrite the spin-flip SANS cross section for the perpendicular scattering geometry [see Fig. 1 and Eq. (4)] as follows:

$$\frac{d\Sigma_{\mathrm{sf}}}{d\Omega}(\mathbf{q}) = K \left(\widetilde{\Gamma}^{xx} + \widetilde{\Gamma}^{yy} \cos^4\theta + \widetilde{\Gamma}^{zz} \sin^2\theta \cos^2\theta - [\widetilde{\Gamma}^{yz} + \widetilde{\Gamma}^{zy}] \sin\theta \cos^3\theta \right), \tag{42}$$

with $\mathbf{q} = q[0, \sin\theta, \cos\theta]$. We emphasize that the $\widetilde{\Gamma}^{\iota\kappa}$ are functions of q and θ. In the following discussion, we focus on the first-order approximation and we neglect interparticle interaction effects.

B. First-order approximation for a dilute ensemble of spherical nanoparticles

For a dilute ($\mathbf{a}_{\nu} = \mathbf{a}_{\mu}$) and monodisperse ($\widetilde{S}_{\nu} = \widetilde{S}_{\mu} = \widetilde{S}$) ensemble of spherical nanoparticles (with radius R), the Fourier cross-correlation functions simplify to [6]:

$$\widetilde{\Gamma}^{\iota\kappa}(\mathbf{q}) = i^{|\boldsymbol{\alpha}|-|\boldsymbol{\beta}|} M^{\iota}_{\mu,\boldsymbol{\alpha}} M^{\kappa}_{\mu,\boldsymbol{\beta}} \partial^{\boldsymbol{\alpha}} \widetilde{S}(q) \partial^{\boldsymbol{\beta}} \widetilde{S}(q), \tag{43}$$

where $q = \sqrt{q_x^2 + q_y^2 + q_z^2}$, and

$$\widetilde{S}(q) = \frac{3V_{\mathrm{s}}}{(2\pi)^{3/2}} \frac{j_1(qR)}{qR} \quad \text{with} \quad V_{\mathrm{s}} = \frac{4\pi R^3}{3}. \tag{44}$$

$j_1(u) = \sin u/u^2 - \cos u/u$ is the first-order spherical Bessel function. In this special case of spherical nanoparticles (where $\widetilde{S} = \widetilde{S}^{*}$), the Fourier transform of the indicator function becomes real-valued, such that it is obvious that only terms with $|\boldsymbol{\alpha}| - |\boldsymbol{\beta}| = 2u$ (with $u \in \mathbb{Z}$) contribute to Eq. (43) [13]. In the study of Adams et. al. [14], the zero-order case of Eq. (43), which reflects a dilute and monodisperse ensemble of uniformly magnetized spherical nanoparticles, was studied in the context of the Stoner-Wohlfarth model. In this situation, the cross-correlation matrix can be written as:

$$\widetilde{\Gamma}^{\iota\kappa}(\mathbf{q}) = \Gamma_0^{\iota\kappa} [\widetilde{S}(q)]^2 \quad \text{with} \quad \Gamma_0^{\iota\kappa} = M^{\iota}_{\nu,(0,0,0)} M^{\kappa}_{\nu,(0,0,0)}. \tag{45}$$

The real-space cross-correlation matrix $\Gamma_0^{\iota\kappa}$ is a function of the applied magnetic field, such that the two-dimensional magnetic SANS cross section exhibits different types of angular anisotropies, even for randomly-averaged ensembles at remanence or at the coercive field [14].

Now, taking into account spin inhomogeneities up to the first polynomial order in the expansion of the magnetization [Eq. (36)], Eq. (43) becomes:

$$\widetilde{\Gamma}^{\iota\kappa}(\mathbf{q}) = \Gamma_0^{\iota\kappa}\widetilde{S}^2 + \Gamma_{1,lm}^{\iota\kappa}\left[\frac{\partial\widetilde{S}}{\partial q_l}\right]\left[\frac{\partial\widetilde{S}}{\partial q_m}\right], \tag{46}$$

where we have defined the combinations of polynomial magnetization coefficients as:

$$\Gamma_0^{\iota\kappa} = M^{\iota}_{\nu,\boldsymbol{F}_0} M^{\kappa}_{\nu,\boldsymbol{F}_0}, \tag{47}$$

$$\Gamma_{1,\ell m}^{\iota\kappa} = M^{\iota}_{\nu,\boldsymbol{F}_\ell} M^{\kappa}_{\nu,\boldsymbol{F}_m}, \tag{48}$$

and we use the following $\boldsymbol{F}_i$ symbol for booking the multi-indices of the magnetization coefficients:

$$\boldsymbol{F}_i = \begin{cases} (0,0,0) & , i = 0 \\ (1,0,0) & , i = x \\ (0,1,0) & , i = y \\ (0,0,1) & , i = z \end{cases}. \tag{49}$$

We note that the new Γ and C coefficients include the sum over the ensemble of nanoparticles. This is seen from the fact that the index ν occurs only on the right-hand-side of Eqs. (47) and (48), but not on the left-hand-side. Since (for a spherical particle) the Fourier transform of the indicator function $\widetilde{S}$ depends only $q = \sqrt{q_x^2 + q_y^2 + q_z^2}$, we can express the partial derivatives of $\widetilde{S}$ in Eq. (46) (using the chain rule) up to the first-order as:

$$\widetilde{S}(q) = \frac{3V_\mathrm{s}}{(2\pi)^{3/2}}\frac{j_1(qR)}{qR}, \qquad \frac{\partial\widetilde{S}}{\partial q_\alpha} = \hat{q}_\alpha \widetilde{S}' \tag{50}$$

where $\hat{q}_l = q_l/q$ (with $l = x, y, z$), $\delta^{\alpha\beta}$ is the Kronecker delta symbol, and the prime denotes the derivative with respect to the radial coordinate, i.e., $\widetilde{S}' = d\widetilde{S}/dq$ and $\widetilde{S}'' = d^2\widetilde{S}/dq^2$. Using the results from Eq. (50), we can rewrite Eq. (46) as follows:

$$\widetilde{\Gamma}^{\iota\kappa}(\mathbf{q}) = \Gamma_0^{\iota\kappa}\widetilde{S}^2 + \Gamma_{1,\ell m}^{\iota\kappa}\hat{q}^\ell\hat{q}^m\widetilde{S}'^2. \tag{51}$$

In the above formulation, we see that the angular ($\hat{q}_\alpha$) dependence and the radial (q) dependence of the cross-correlation functions are separated in the sense of a multiplication. This is an important property that facilitates the further calculations, especially the azimuthal averaging of the magnetic SANS cross section (see below). Furthermore, inspection of Eq. (50) shows that the shape function $\widetilde{S}$ and its ordinary derivatives with respect to the radial coordinate q also depend on the radius R of the particle. Therefore, it is convenient to define the dimensionless function $f(u = qR)$ such that the shape function $\widetilde{S}$ and its derivatives can be written as follows:

$$f(u) = \frac{j_1(u)}{u} = \frac{\sin u - u\cos u}{u^3}, \qquad \widetilde{S}(q) = \frac{3V_\mathrm{s}}{(2\pi)^{3/2}}f(qR), \tag{52}$$

$$f'(u) = \frac{(u^2-3)\sin u + 3u\cos u}{u^4}, \qquad \widetilde{S}'(q) = \frac{3V_\mathrm{s}R}{(2\pi)^{3/2}}f'(qR). \tag{53}$$

In order to write the cross-correlation matrix [Eq. (51)] in compact form, we introduce the following radial functions g_k and angular functions $G_k^{\iota\kappa}$:

$$g_0(u) = (f(u))^2, \qquad G_0^{\iota\kappa}(\hat{\mathbf{q}}) = h\Gamma_0^{\iota\kappa}, \tag{54}$$

$$g_1(u) = (f'(u))^2, \qquad G_1^{\iota\kappa}(\hat{\mathbf{q}}) = hR^2\Gamma_{1,\ell m}^{\iota\kappa}\hat{q}^\ell\hat{q}^m, \tag{55}$$

The functions $g_0(u)$ and $g_1(u)$ are shown in Fig. 5. For completeness we provide the limit of the functions $g_i(u)$ for $u \to 0$:

$$\lim_{u\to 0} g_0(u) = \frac{1}{9} \qquad \lim_{u\to 0} g_1(u) = 0. \tag{56}$$

The azimuthally-averaged spin-flip SANS cross section $I_\mathrm{sf}(q)$ for the perpendicular scattering geometry is then obtained by a projection onto the two-dimensional detector plane, i.e., setting $\hat{\mathbf{q}} = [0, \sin\theta, \cos\theta]$ in Eq. (51). Substituting

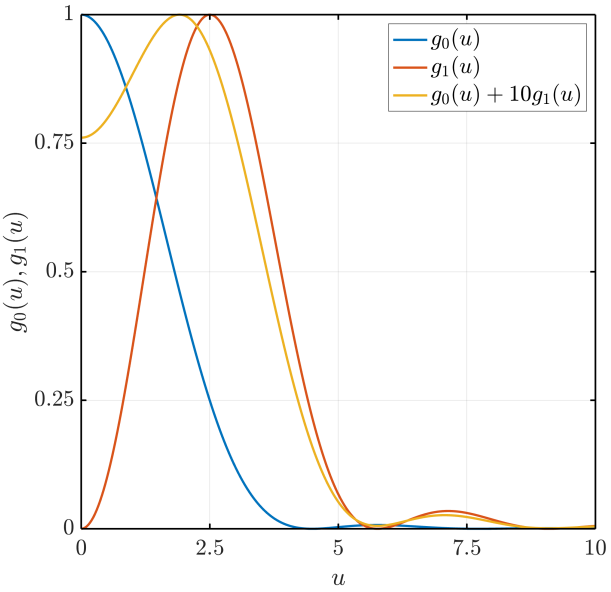

FIG. 5. The functions $g_0(u)$, $g_1(u)$, and their weighted sum. The functions are normalized to their maximum values.

Eq. (51) for the $\widetilde{\Gamma}^{\iota\kappa}(\mathbf{q})$ into Eq. (72) and carrying out an azimuthal average $[(2\pi)^{-1}\int_0^{2\pi}(...)d\theta]$, we obtain [Eq. (1) in the main text]

$$I_{\rm sf}(q) = I_{\rm sf}^0\left[\frac{\sin(qR)-qR\cos(qR)}{q^3R^3}\right]^2 + I_{\rm sf}^1\left[\frac{(q^2R^2-3)\sin(qR)+3qR\cos(qR)}{q^4R^4}\right]^2, \tag{57}$$

where the $I_{\rm sf}^k$ are constant prefactors

$$I_{\rm sf}^k = \frac{1}{2\pi}\frac{8\pi^3 b_{\rm H}^2}{V}\int_0^{2\pi}\left(G_k^{xx}+G_k^{yy}\cos^4\theta+G_k^{zz}\sin^2\theta\cos^2\theta-(G_k^{yz}+G_k^{zy})\sin\theta\cos^3\theta\right)\,d\theta. \tag{58}$$

The first term in Eq. (57) corresponds to the form factor of a uniformly magnetized sphere, and the second term is the first-order extension. The zero- and first-order coefficients $I_{\rm sf}^0$ and $I_{\rm sf}^1$, as functions of the correlation coefficients Γ, are given by

$$I_{\rm sf}^0 = \frac{9V_{\rm s}^2 b_{\rm H}^2}{8V}\left(8\Gamma_0^{xx}+3\Gamma_0^{yy}+\Gamma_0^{zz}\right), \tag{59}$$

$$I_{\rm sf}^1 = \frac{9V_{\rm s}^2 R^2 b_{\rm H}^2}{16V}\left(8\Gamma_{1,yy}^{xx}+8\Gamma_{1,zz}^{xx}+\Gamma_{1,yy}^{yy}+5\Gamma_{1,zz}^{yy}+\Gamma_{1,yy}^{zz}+\Gamma_{1,zz}^{zz}-2\Gamma_{1,yz}^{yz}-2\Gamma_{1,zy}^{yz}\right). \tag{60}$$

In the perfectly saturated state, the higher-order coefficients in Eq. (57) vanish and the remaining zeroth-order term is given by:

$$I_{\rm sf}(q;B_0\to\infty) = I_{\rm sf}^{0,\rm sat}g_0(qR) = I_{\rm sf}^{0,\rm sat}\left[\frac{j(qR)}{qR}\right]^2. \tag{61}$$

The corresponding spin-flip pair-distance distribution function $p_{\rm sf}(r)$ is then obtained from the spherical Hankel transform of $I_{\rm sf}(q)$ [Eq. (57)] as:

$$\begin{aligned} p_{\rm sf}(r) &= r^2\int_0^\infty I_{\rm sf}(q)j_0(qr)q^2dq \\ &= I_{\rm sf}^0\frac{\pi r^2}{6R^3}\left[1-\frac{3r}{4R}+\frac{r^3}{16R^3}\right] + I_{\rm sf}^1\frac{\pi r^2}{10R^3}\left[1-\frac{5r}{4R}+\frac{5r^3}{16R^3}-\frac{r^5}{32R^5}\right]. \end{aligned} \tag{62}$$

Here, the first term corresponds to the well-known pair-distance distribution function of a uniformly magnetized spherical nanoparticle, whereas the second term represents the first-order extension, with the ability to describe

vortex-like spin textures. For completeness, we remind the reader that the general boundary conditions for the pair-distance distribution function Eq. (62) in the case of objects of finite size are given by:

$$p_{\rm sf}(0) = 0, \qquad p_{\rm sf}(2R) = 0, \tag{63}$$

$$\left.\frac{dp_{\rm sf}}{dr}\right|_{r=0} = 0, \qquad \left.\frac{dp_{\rm sf}}{dr}\right|_{r=2R} = 0. \tag{64}$$

Figure 1 in the main paper displays the "phase diagram" for $I_{\rm sf}(q)$ and $p_{\rm sf}(r)$. Plotted are Eqs. (57) and (62) as functions of the ratio $I^1_{\rm sf}/I^0_{\rm sf}$. Already for $I^1_{\rm sf}/I^0_{\rm sf} > 1$, we find that $p_{\rm sf}(r)$ exhibits negative values above a certain distance r. The presence of negative values in the pair-distance distribution function (as well as in the correlation function) refers to antiparallel spin correlations. Therefore, such negative values are a strong indication for the presence of vortex-type spin structures. For even larger values of $I^1_{\rm sf}/I^0_{\rm sf}$, the distance distribution function reveals a damped oscillatory behavior with the zero crossing shifting to smaller r. This observation is accompanied by the appearance of a maximum in $I_{\rm sf}(q)$ at a certain momentum transfer q that is different from $q = 0$. The transition point above which $I_{\rm sf}(q)$ shows a reduced behavior at $q = 0$ is given by a coefficient ratio $I^1_{\rm sf}/I^0_{\rm sf} > 5$.

We emphasize that in this formulation of the neutron-scattering observables it is only assumed that the magnetization vector field is of linear polynomial order. In the following, we derive analytical results for the specific case that this linear polynomial takes on the form of a vortex.

IV. LINEAR THEORY FOR VORTEX SPIN STRUCTURES

For the particular case of a linear vortex profile, analytical expressions for $d\Sigma_{\rm sf}/d\Omega$ and chiral function $d\Sigma_\chi/d\Omega$ can be derived. For this, we assume that the magnetization vector field (for $r < R$) can be written as:

$$\mathbf{M}'(\mathbf{r}') = m_0\mathbf{e}'_z + m_1\mathbf{v}(\mathbf{r}'), \tag{65}$$

where $\mathbf{e}'_z = [0, 0, 1]$ is the unit vector in z' direction, $\mathbf{v}(\mathbf{r}') = [-y', x', 0]$ is the linear vortex field, and $\mathbf{r}' = [x', y', z']$ is the position vector with reference to the local vortex frame. A positive value for m_1 indicates a counterclockwise (CCW) or right-handed sense of rotation, while a negative m_1 corresponds to a clockwise (CW) or left-handed sense of rotation. We note that for a micromagnetic Hamiltonian that contains the isotropic exchange interaction, magnetic anisotropy, and the Zeeman and magnetodipolar interaction there exists no preference for CCW or CW vortex rotation senses in the particles. CCW and CW vortices appear with equal probability so that the chiral function averages to zero (see below). By including the Dzyaloshinskii-Moriya interaction (DMI), which breaks space-inversion symmetry, chirality selection takes place and leads to a nonzero chiral function [15]. Applying the Fourier differentiation theorem, we obtain the following expression for the Fourier transform of the above local magnetization vector field:

$$\widetilde{\mathbf{M}}'(\mathbf{q}') = [-\mathrm{i}m_1\partial_{q_y}\widetilde{S}(q'),\ \mathrm{i}m_1\partial_{q'_x}\widetilde{S}(q'),\ m_0\widetilde{S}(q)], \tag{66}$$

where $\widetilde{S}$ denotes the spherical form-factor function

$$\widetilde{S}(q) = \frac{3V_{\rm s}}{(2\pi)^{3/2}}\frac{\sin(qR) - qR\cos(qR)}{q^3R^3}. \tag{67}$$

Using the chain rule we find:

$$\widetilde{\mathbf{M}}'(\mathbf{q}') = [-\mathrm{i}m_1\hat{q}'_y S'(q),\ \mathrm{i}m_1\hat{q}'_x S'(q'),\ m_0 S(q')] \tag{68}$$

with

$$\widetilde{S}'(q) = \frac{d\widetilde{S}}{dq} = \frac{3V_{\rm s}}{(2\pi)^{3/2}}\frac{(q^2R^2 - 3)\sin(qR) + 3qR\cos(qR)}{q^4R^4}, \tag{69}$$

and $\hat{q}_\nu = q_\nu/q$ denotes the normalized Fourier space coordinates. We assume a dilute assembly of spherical nanoparticles with randomly-distributed orientations of the magnetocrystalline anisotropy. In this case, the magnetization vector field in the local particle frame [Eq. (65)] needs to be transformed into the global laboratory frame of reference by a zy rotation matrix $\mathbf{R}(\alpha, \beta) = \mathbf{R}_z(\beta) \cdot \mathbf{R}_y(\alpha)$, where α is the polar angle and β the azimuth angle. Such a rotation transformation is invariant when going from real space to Fourier space, which is why the transformation of the magnetization in Fourier space is transformed as:

$$\widetilde{\mathbf{M}}(\mathbf{q}; \alpha, \beta) = \mathbf{R}(\alpha, \beta) \cdot \widetilde{\mathbf{M}}'\left(\mathbf{R}^T(\alpha, \beta) \cdot \mathbf{q}\right). \tag{70}$$

Using the following definition of the correlation matrix of the Fourier magnetization vector field,

$$\widetilde{\Gamma}^{\iota\kappa}(\mathbf{q}) = \left[\widetilde{M}^{\iota}(\mathbf{q})\right]\left[\widetilde{M}^{\kappa}(\mathbf{q})\right]^{*}, \tag{71}$$

and by projection into the detector plane $\mathbf{q} = [0, q\sin\theta, q\cos\theta]$, the spin-flip SANS cross section $\frac{d\Sigma_{\rm sf}}{d\Omega}(q,\theta;\alpha,\beta)$ and the chiral function $\frac{d\Sigma_{\chi}}{d\Omega}(q,\theta;\alpha,\beta)$ corresponding to a single nanoparticle with vortex orientation (α,β) are written as (see also [8]):

$$\frac{d\Sigma_{\rm sf}}{d\Omega}(q,\theta;\alpha,\beta) = K\left[\widetilde{\Gamma}^{xx} + \widetilde{\Gamma}^{yy}\cos^4\theta + \widetilde{\Gamma}^{zz}\sin^2\theta\cos^2\theta - (\widetilde{\Gamma}^{yz} + \widetilde{\Gamma}^{zy})\sin\theta\cos^3\theta\right], \tag{72}$$

$$\frac{d\Sigma_{\chi}}{d\Omega}(q,\theta;\alpha,\beta) = K\left[(\widetilde{\Gamma}^{xy} - \widetilde{\Gamma}^{yx})\cos^2\theta + (\widetilde{\Gamma}^{xz} - \widetilde{\Gamma}^{zx})\sin\theta\cos\theta\right]. \tag{73}$$

In the MNPSE method, we define the ensemble-averaged (dilute) SANS cross sections as:

$$\left\langle \frac{d\Sigma_{\rm sf,\chi}}{d\Omega} \right\rangle = \frac{1}{2}\int_0^{4\pi}\left[\frac{d\Sigma_{\rm sf,\chi}^{\rm CCW}}{d\Omega} + \frac{d\Sigma_{\rm sf,\chi}^{\rm CW}}{d\Omega}\right]\psi(\alpha,\beta)d\Upsilon \tag{74}$$

where $d\Upsilon = \sin\alpha d\alpha d\beta$ is the solid-angle differential, and $\frac{d\Sigma_{\rm sf,\chi}^{\rm CCW}}{d\Omega}(\mathbf{q};\alpha,\beta)$ and $\frac{d\Sigma_{\rm sf,\chi}^{\rm CW}}{d\Omega}(\mathbf{q};\alpha,\beta)$ are the SANS cross sections referring to two nanoparticles with the same orientation (α,β), but opposite senses of vortex rotation ($m_1^{\rm CCW} = -m_1^{\rm CW}$). The function $\psi(\alpha,\beta)$ is a field-dependent probability distribution modelling the orientation of both the CCW and CW vortex rotation axes (no distinction between the different polarities). For simplicity, we assume a uniform distribution $\psi_{\rm u}$ on the spherical surface, which is limited by a field-dependent conical opening angle $0° \leq \alpha_{\rm c} \leq 90°$. The azimuthally-symmetric distribution function is then given by:

$$\psi_{\rm u}(\alpha,\beta) = \frac{\Theta(1-\alpha/\alpha_c)}{2\pi(1-\cos\alpha_{\rm c})}, \tag{75}$$

where $\Theta(\xi)$ is the Heaviside function. Finally, the resulting spin-flip SANS cross section and chiral function for a dilute ensemble of spherical nanoparticles with vortex type spin structures reads ($\mathbf{H}_0 \perp \mathbf{k}_0$):

$$\begin{aligned}\left\langle \frac{d\Sigma_{\rm sf}}{d\Omega} \right\rangle(q,\theta) = {}& \frac{W}{8}[m_0 f(qR)]^2 \times \left[12 - (\cos^2\alpha_{\rm c} + \cos\alpha_{\rm c})(3\cos^2(2\theta) + 2\cos(2\theta) + 3) + 4\cos(2\theta)\right] \\ & + \frac{W}{2}[m_1 R f'(qR)]^2 \times \left[3 - (2\cos^2\alpha_{\rm c} + 2\cos\alpha_{\rm c} - 1)\cos(2\theta)\right],\end{aligned} \tag{76}$$

$$\left\langle \frac{d\Sigma_{\chi}^{\rm CCW,CW}}{d\Omega} \right\rangle(q,\theta) = \pm W\left[m_0|m_1|Rf(qR)f'(qR)\cos\theta\right] \times \left[4 + \cos^2\alpha_{\rm c} + \cos\alpha_{\rm c} - 3(\cos^2\alpha_{\rm c} + \cos\alpha_{\rm c})\cos^2\theta\right], \tag{77}$$

where $W = 3V_{\rm s}^2 b_{\rm H}^2/V$. The "+" sign in Eq. (77) stands for CCW and the "−" sign for CW vortex rotations. Equations (76) and (77) are displayed in Fig. 2 in the main paper. When no chirality selection takes place, then it follows that:

$$\left\langle \frac{d\Sigma_{\chi}}{d\Omega} \right\rangle = \frac{1}{2}\left[\left\langle \frac{d\Sigma_{\chi}^{\rm CCW}}{d\Omega} \right\rangle + \left\langle \frac{d\Sigma_{\chi}^{\rm CW}}{d\Omega} \right\rangle\right] = 0. \tag{78}$$

The azimuthally-averaged spin-flip SANS cross section then equals:

$$\begin{aligned}\langle I_{\rm sf}\rangle(q) &= \frac{1}{2\pi}\int_0^{2\pi}\left\langle \frac{d\Sigma_{\rm sf}}{d\Omega} \right\rangle(q,\theta)d\theta \\ &= \frac{3W}{16}\left([m_0 f(qR)]^2(8 - 3\cos^2\alpha_{\rm c} - 3\cos\alpha_{\rm c}) + 8[m_1 R f'(qR)]^2\right).\end{aligned} \tag{79}$$

Comparing this expression to Eq. (57) we find:

$$I_{\rm sf}^0 = \frac{3W}{16}m_0^2(8 - 3\cos^2\alpha_{\rm c} - 3\cos\alpha_{\rm c}), \tag{80}$$

$$I_{\rm sf}^1 = \frac{3W}{16}8m_1^2R^2, \tag{81}$$

$$\iota = \frac{I_{\rm sf}^1}{I_{\rm sf}^0} = \frac{8m_1^2R^2}{m_0^2(8 - 3\cos^2\alpha_{\rm c} - 3\cos\alpha_{\rm c})}. \tag{82}$$

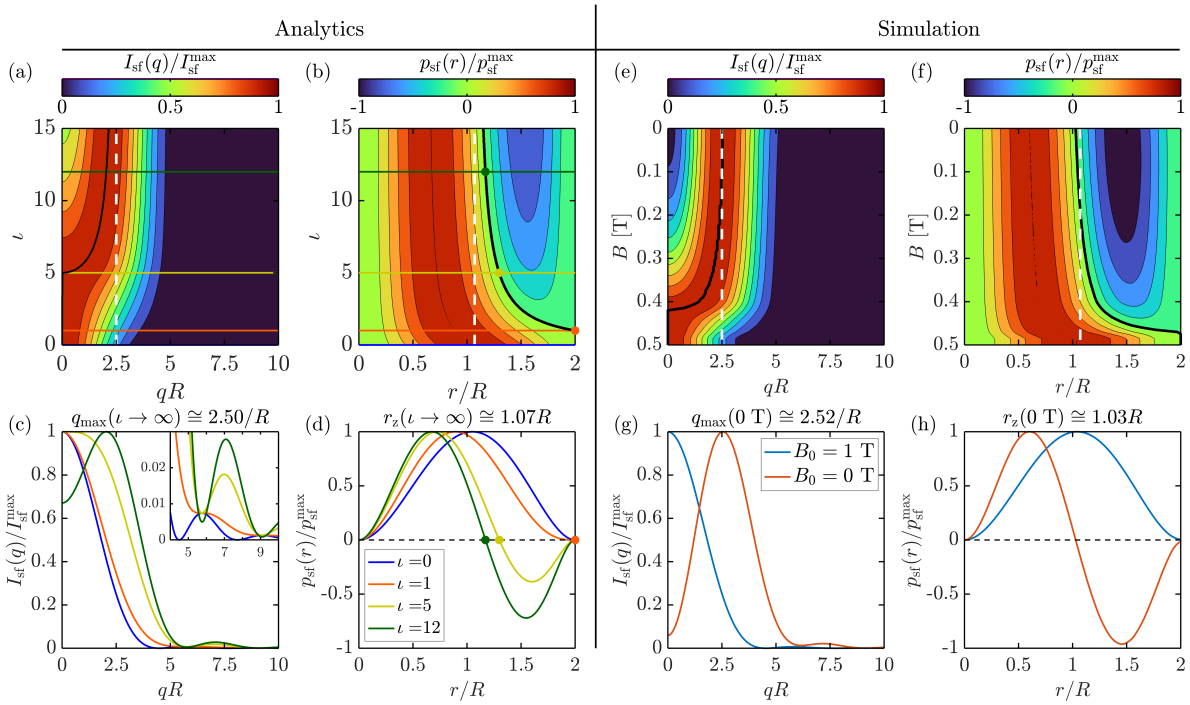

FIG. 6. Same as Fig. 1 in the main paper, but for a uniaxial particle anisotropy (1600 random orientations). "Phase diagram" for the azimuthally-averaged spin flip SANS cross section $I_{\rm sf}(q)$ [Eq. (57)] and for the spin-flip pair-distance distribution function $p_{\rm sf}(r)$ [Eq. (62)] within the limits of the first-order magnetization model. The left panel shows the analytical results, while the right panel features the corresponding results of the micromagnetic simulations. The ratio ι of the zero-order coefficient $I_{\rm sf}^0$ and the first-order coefficient $I_{\rm sf}^1$ determines the appearance of vortex-type spin structures. Field ($B_0=\mu_0 H_0$) variations in the simulations correspond to ι variations in the analytical part (zero field: $\iota\to\infty$; saturation: $\iota\to 0$). (a) Color-coded plot of the normalized $I_{\rm sf}(q)$ as a function of $\iota=I_{\rm sf}^1/I_{\rm sf}^0$ and qR. The black solid line in (a) describes the shift of the maximum in $I_{\rm sf}(q)$ towards $q_{\rm max}\cong 2.50/R$ [white dashed line, compare (e)]. (b) Normalized $p_{\rm sf}(r)$ as a function of ι and r/R. The black solid line in (b) describes the shift of the zero in $p_{\rm sf}(r)$ towards $r_{\rm z}\cong 1.07R$ [white dashed line, compare (f)]. (c) Normalized $I_{\rm sf}(qR)$ and (d) normalized $p_{\rm sf}(r/R)$ for different ι [see inset in (d)]; the inset in (c) displays $I_{\rm sf}(q)/I_{\rm sf}^{\rm max}$ for $4<qR<10$. The colored horizontal lines in (a) and (b) correspond, respectively, to the curves in (c) and (d).

V. UNIAXIAL VERSUS CUBIC RANDOM ANISOTROPY

The micromagnetic simulation results that are reported in the main paper were carried out using the materials parameters of iron, which possesses a cubic magnetocrystalline anisotropy. Figures 6−9 show the results when a random uniaxial anisotropy is used in the simulations, instead of a random cubic anisotropy. More specifically, the following expression for the magnetic anisotropy energy has been used [replacing Eq. (14)]:

$$E_{\rm ani}=-K_{\rm u1}\int(\mathbf{e}_{\rm A}\cdot\mathbf{m})^2\,dV, \tag{83}$$

where $K_{\rm u1}=+4.7\times10^4\,{\rm J/m^3}$ denotes the first-order uniaxial anisotropy constant, and $\mathbf{e}_{\rm A}$ is a unit vector specifying the local random easy-axis direction of a particle. Comparing Figs. 6 and 7 with Figs. 1 and 2 in the main paper, and likewise Figs. 2 and 3 with Figs. 8 and 9, see that the behavior is qualitatively and quantitatively very similar.

We acknowledge financial support from the National Research Fund of Luxembourg (AFR Grant No. 15639149, CORE Grant DeQuSky, and PRIDE MASSENA Grant).

[1] D. Honecker, A. Ferdinand, F. Döbrich, C. D. Dewhurst, A. Wiedenmann, C. Gómez-Polo, K. Suzuki, and A. Michels, Eur. Phys. J. B **76**, 209 (2010).
[2] K. L. Krycka, J. A. Borchers, R. A. Booth, Y. Ijiri, K. Hasz, J. J. Rhyne, and S. A. Majetich, Phys. Rev. Lett. **113**, 147203 (2014).

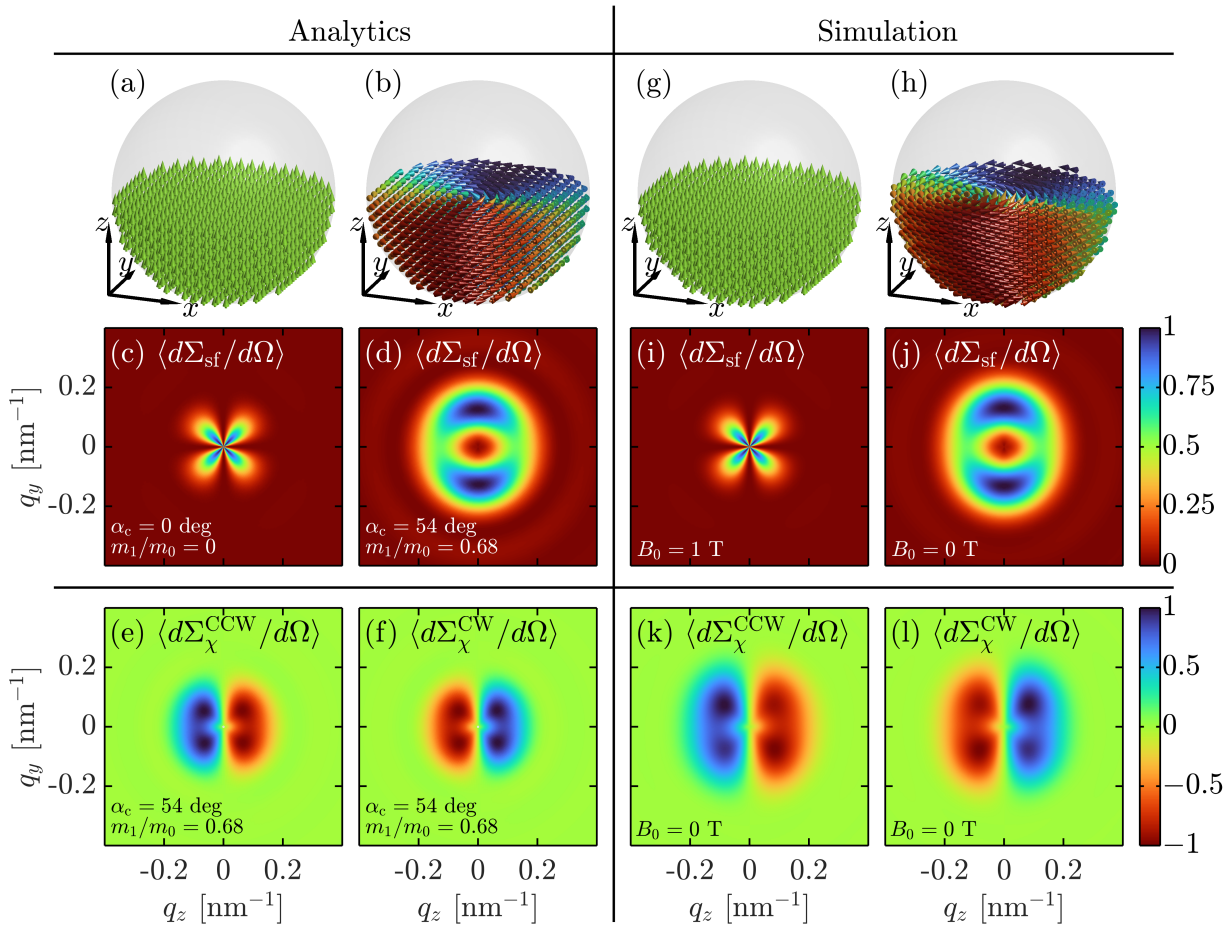

FIG. 7. Same as Fig. 2 in the main paper, but for a uniaxial particle anisotropy (1600 random orientations). Illustration of the 2D (normalized) spin-flip SANS cross section and chiral function computed from Eqs. (76) and (77) reflecting the saturation and remanence cases (particle size: $D = 2R = 40\,\text{nm}$) (linear color scale). (a,b) and (g,h) show snapshots of the underlying real-space spin structures. The left panel shows the analytical results, while the right panel features the results of the micromagnetic simulations. The incoming neutron beam is perpendicular to the applied magnetic field $\mathbf{H}_0 \parallel \mathbf{e}_z$ ($B_0 = \mu_0 H_0$). The maximum of the spots in (d) and (j) are found at $q_{y,\max} \cong 2.50/R$. (e,f) and (k,l) display the respective chiral functions in the remanent state for counterclockwise (CCW) and clockwise (CW) vortex rotations. Note that the specific values for $\alpha_{\rm c} = 54°$ and for the ratio $m_1/m_0 = 0.68$ in (d) are based on a fit of the analytical function [Eq. (76)] to the 2D simulation data shown in (j).

[3] D. Zákutná, D. Nižňanský, L. C. Barnsley, E. Babcock, Z. Salhi, A. Feoktystov, D. Honecker, and S. Disch, Phys. Rev. X **10**, 031019 (2020).
[4] C. Kons, K. L. Krycka, J. Robles, N. Ntallis, M. Pereiro, M.-H. Phan, H. Srikanth, J. A. Borchers, and D. A. Arena, ACS Appl. Nano Mater. **6**, 10986 (2023).
[5] V. Ukleev, F. Ajejas, A. Devishvili, A. Vorobiev, N.-J. Steinke, R. Cubitt, C. Luo, R.-M. Abrudan, F. Radu, V. Cros, N. Reyren, and J. S. White, STAM Methods **25**, 2315015 (2024).
[6] A. Michels, *Magnetic Small-Angle Neutron Scattering: A Probe for Mesoscale Magnetism Analysis* (Oxford University Press, Oxford, 2021).
[7] M. P. Adams, A. Michels, and H. Kachkachi, J. Appl. Cryst. **55**, 1488 (2022).
[8] M. P. Adams, E. P. Sinaga, H. Kachkachi, and A. Michels, Phys. Rev. B **109**, 024429 (2024).
[9] A. Vansteenkiste, J. Leliaert, M. Dvornik, M. Helsen, F. Garcia-Sanchez, and B. Van Waeyenberge, AIP Advances **4**, 107133 (2014).
[10] J. Leliaert, M. Dvornik, J. Mulkers, J. De Clercq, M. V. Milošević, and B. Van Waeyenberge, J. Phys. D: Appl. Phys. **51**, 123002 (2018).
[11] W. F. Brown Jr., *Micromagnetics* (Interscience Publishers, New York, 1963).
[12] In the simulations, $\mathbf{c}_1$ is a random unit vector that is generated using two random angles. A second random unit vector, say $\mathbf{b}$, is generated by another set of random angles, such that $\mathbf{c}_2 = (\mathbf{c}_1 \times \mathbf{b})/|\mathbf{c}_1 \times \mathbf{b}|$ and $\mathbf{c}_3 = \mathbf{c}_1 \times \mathbf{c}_2$.
[13] This follows from the fact that the SANS cross section is a real-valued quantity.

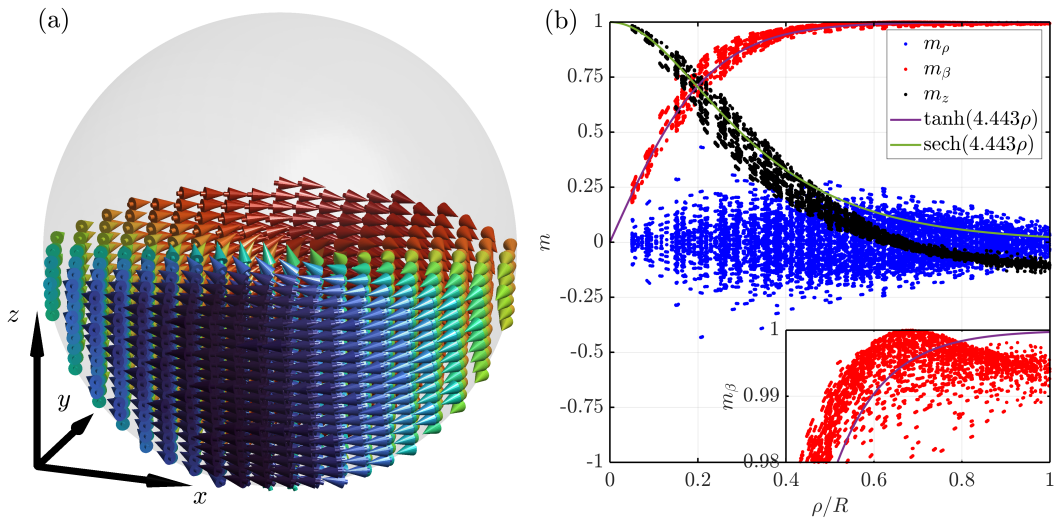

FIG. 8. Same as Fig. 2, but for a uniaxial particle anisotropy (1600 random orientations).

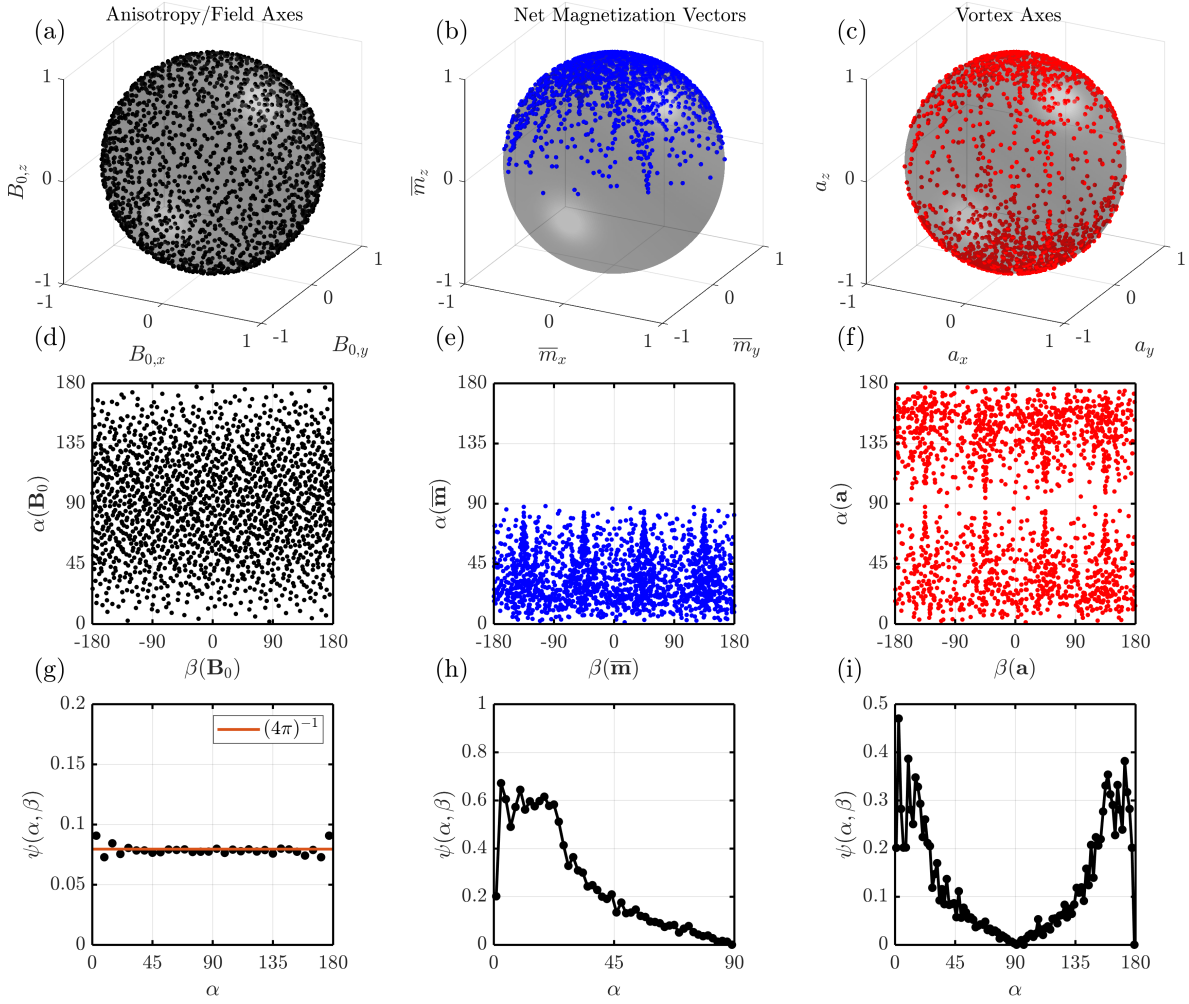

FIG. 9. Same as Fig. 3, but for a uniaxial particle anisotropy (1600 random orientations).

[14] M. P. Adams, E. P. Sinaga, and A. Michels, IUCrJ **10**, 261 (2023).

[15] E. P. Sinaga, M. P. Adams, E. H. Hasdeo, and A. Michels, (2024), arXiv:2402.00558 [cond-mat.mes-hall].